A CONTROL MOMENT GYROSCOPE BASED ON ROTATIONAL VIBRATIONS, DYNAMIC MODEL AND EXPERIMENTATION

A THESIS SUBMITTED TO
THE GRADUATE SCHOOL OF NATURAL AND APPLIED SCIENCES
OF
MIDDLE EAST TECHNICAL UNIVERSITY

BY

FERHAT ARBERKLI

IN PARTIAL FULFILLMENT OF THE REQUIREMENTS
FOR
THE DEGREE OF MASTER OF SCIENCE
IN
MECHANICAL ENGINEERING

SEPTEMBER 2018

Approval of the thesis:

A CONTROL MOMENT GYROSCOPE BASED ON ROTATIONAL VIBRATIONS, DYNAMIC MODEL AND EXPERIMENTATION

submitted by **FERHAT ARBERKLI** in partial fulfillment of the requirements for the degree of **Master of Science in Mechanical Engineering Department, Middle East Technical University** by,

Prof. Dr. Halil Kalıpçılar
Dean, Graduate School of **Natural and Applied Sciences** _____

Prof. Dr. Sahir Arıkan
Head of Department, **Mechanical Engineering** _____

Assist. Prof. Dr. Kıvanç Azgın
Supervisor, **Mechanical Engineering, METU** _____

Examining Committee Members:

Assoc. Prof. Dr. Ergin Tönük
Mechanical Engineering Dept., METU _____

Assist. Prof. Dr. Kıvanç Azgın
Mechanical Engineering, METU _____

Prof. Dr. Kemal Özgören
Mechanical Engineering Dept., METU _____

Prof. Dr. Ozan Tekinalp
Aerospace Engineering Dept., METU _____

Assist. Prof. Dr. Kutluk Bilge Arıkan
Mechanical Engineering, TED University _____

Date: 07.09.2018

I hereby declare that all information in this document has been obtained and presented in accordance with academic rules and ethical conduct. I also declare that, as required by these rules and conduct, I have fully cited and referenced all material and results that are not original to this work.

Name, Surname: Ferhat Arberkli

Signature:

ABSTRACT

A CONTROL MOMENT GYROSCOPE BASED ON ROTATIONAL VIBRATIONS, DYNAMIC MODEL AND EXPERIMENTATION

Arberkli, Ferhat
Master of Science, Mechanical Engineering
Supervisor: Assist. Prof. Dr. Kıvanç Azgın

September 2018, 74 pages

Satellite attitude determination and control system is one of the main subsystems of a spacecraft. Within this domain, there are several types of actuators; such as reaction wheels, control moment gyroscopes (CMG), propulsion systems and magnetic torque rods. All of them are common and currently being used on modern satellites and space stations depending on the application. Conventional reaction wheel and CMG operation are based on the continuous rotation of their rotor mass to exchange angular momentum between spacecraft body and their rotor body. It this thesis, vibration is proposed as a new way of actuation instead of continuous rotation. Firstly, a mathematical model of single axis vibrating CMG was developed and the possibility of useful output is investigated. Effects of system excitation parameters were analyzed and interpreted. In addition, unwanted vibrations on spacecraft due to excitation responses were canceled, and performance of the actuator was improved by finding optimum rotor geometry. Finally, two experimentation setups were designed, manufactured, tested and their results were discussed.

Keywords: Control moment gyroscope, vibration, satellite attitude control

ÖZ

DÖNEL TİTREŞİMLERLE ÇALIŞAN KONTROL MOMENTİ JİROSKOBU, DİNAMİK MODEL VE DENEY

Arberkli, Ferhat
Yüksek Lisans, Makina Mühendisliği
Tez Danışmanı: Dr. Öğr. Üyesi Kıvanç Azgın

Eylül 2018, 74 sayfa

Uydu yönelim tespiti ve kontrolü bir uzay aracının ana alt sistemlerinden birisidir. Bu bağlamda, uydu yönelimini sağlayan tepki tekeri, kontrol momenti jiroskobu (KMJ), itki sistemi ve manyetik tork çubuğu gibi eyleyiciler vardır. Tüm bu eyleyiciler yaygın bir şekilde günümüz modern uydularında ve uzay istasyonlarında uygulamaya bağlı olarak kullanılmaktadır. Standart bir tepki tekeri ve KMJ, rotor adı verilen bir kütlenin sürekli olarak dönmesi ve bu sayede bu kütle ile uzay aracının kütlesi arasında açısal momentum değişimi prensibine dayanarak çalışmaktadır. Bu tezde, sürekli olarak dönme yerine titreşim ile eyleyicinin çalışması önerilmiştir. İlk olarak, titreşimle çalışan tek dengeleme halkalı (gimbal) bir KMJ'nun matematiksel modeli geliştirilmiş ve faydalı bir dönüş elde edilip edilemediği değerlendirilmiştir. Uygulanan titreşim parametrelerinin sistemin açısal hız çıktısına etkisi incelenmiş ve değerlendirilmiştir. Buna ek olarak, uzay aracı üzerinde oluşan istenmeyen titreşimler ortadan kaldırılmış ve en iyi rotor geometrisi tespit edilip eyleyicinin performansı iyileştirilmiştir. Son olarak, iki adet deney düzeneğinin mekanik tasarımı yapılmış, üretilmiş ve testleri yapılıp elde edilen sonuçlar değerlendirilmiştir.

Anahtar Kelimeler: Kontrol momenti jiroskobu, titreşim, uydu yönelim kontrolü

To My Parents

ACKNOWLEDGMENTS

The author wishes to express his deepest gratitude to his supervisor Assist. Prof. Dr. Kıvanç Azgın and project manager Prof. Dr. Ozan Tekinalp for their guidance, advice, criticism, encouragements, and insight throughout the research.

The author would also like to thank Prof. Dr. Kemal Özgören for building a clear understanding of the theory and mathematics behind the subject of the thesis.

The author would also like to thank Mr. Burak Akbulut for his contributions and collaboration throughout this project.

The author would also like to thank Mustafa Boybey and Aslan Makina Company for precise manufacturing of test prototypes.

Lastly, the author would also like to thank Eyyüp Demirkutlu for his sensitive hand workmanship to modify some parts of electrical circuits for the test of the experiment setup.

This study was supported by Scientific and Technological Research Council of Turkey, Project No: 214M074.

TABLE OF CONTENTS

LIST OF FIGURES

FIGURES

CHAPTER 1

INTRODUCTION AND LITERATURE REVIEW

1.1. Introduction to Spacecraft Dynamics

In this chapter, an introduction to spacecraft dynamics and satellite attitude actuators will be presented. The proposed actuator in this thesis closely relevant to the control moment gyroscopes (CMGs) and this part focuses mostly on CMGs and its historical background. Later, the contribution of this study to the field of attitude control actuators will be discussed.

1.1.1. Spacecraft Attitude Dynamics and Control

This engineering field deals with the orientation of the spacecraft in microgravity environment. The orientation of the spacecraft is critical because some of its subsystems must be directed to a specific orientation in order to operate and work properly. For instance, solar panels should be directed to the sunbeams in order to generate the required power for the spacecraft. Similarly, antennas should be pointed towards ground stations to establish a connection for data transfer. In addition to these, the most critical performance demanding application is targeting optical camera to desired locations. Especially, in the Low Earth Orbit (between 160 km and 2000 km altitude) there are many Earth observation satellites. Mostly, attitude control systems in these satellites must be agile to reach desired orientation in the required time span and must hold spacecraft at this orientation without exceeding desired error limit.

Spacecraft attitude control systems consist of sensors, actuators, controlled plant, and controller. Sensors provide information about the orientation of spacecraft (angular acceleration). They provide direction of other celestial bodies such as Sun and other stars (i.e. star tracker) or magnetic field (magnetometer) in order to calculate the attitude of the spacecraft. Attitude determination algorithms run on onboard computer

of spacecraft to calculate the orientation of spacecraft accurately. Guidance algorithms are utilized to determine target orientation. Hence, the current error could be fed to controllers. Controllers provide the necessary outputs to the actuators by using the inputs from the sensors. Actuators perform useful momentum exchange between spacecraft body and inner mass. Hence, spacecraft may reorient to the desired target or absorb external attitude perturbations [1].

1.1.2. Common Spacecraft Attitude Actuators

As mentioned before attitude actuators are subsystems of attitude control loop. There are several common types of attitude actuators such as magnetic torque rods, propulsion systems, reaction wheels, and control moment gyroscopes.

Magnetic torque rods interact with the Earth's magnetic field using principles of electromagnetism and generate torques on the spacecraft body. Generated torque is limited and highly depended on the location of the spacecraft around Earth due to variance in the magnetic field of the Earth. However, they are useful at the beginning of the mission after launch. When the reaction wheels are not activated yet, initial angular velocities must be reduced. They are also used to decrease angular momentum built on the actuators in time. Lastly, they only work when spacecraft is close to the orbiting planet and there is a planetary magnetic field. For instance, Mars orbiter must use a propulsion system to manage angular momentum on spacecraft due to lack of a magnetic field on Mars [2].

The propulsion system is mainly used for orbit maneuvering. However, it may also be used for attitude control by utilizing thrusters. Using the propulsion system for attitude control is costly because it requires a high amount of propellant to operate for long times.

Reaction wheels exchange angular momentum of spacecraft to reorient it by accelerating or decelerating. They also rotate at a constant angular velocity at idle and provide gyroscopic stiffness to the spacecraft at a certain direction. Reaction wheels

can produce more torque than magnetic torque rods and they are better than magnetic torque rods when precision attitude control of the spacecraft is critical.

Control moment gyroscopes (CMGs) are also momentum exchange devices like reaction wheel for attitude control of spacecraft. Reaction wheels create torques by changing the magnitude of angular momentum vector. But unlike reaction wheels, CMGs change the direction of angular momentum vector inside themselves to create control moment on the spacecraft body.

1.1.3. History of Control Moment Gyroscopes

Using CMGs for attitude control is not a new idea. Utilization of CMG concept was developed in early 20th century. J.S. Lang patented a device which uses gyroscopic stiffness to create restoring moment to aircraft in 1914 [3]. Similarly, E.A. Sperry, founder of Sperry Gyroscope Company, designed a similar device for stabilization of ships in 1917 [4]. Rocket pioneer R.H. Goddard also patented a "Gyroscope Steering Apparatus" in 1936. His main idea while developing this device was control of heading of the vehicle which "will be operative regardless of the density of the air through which the craft is moving". His invention is the first implementation of a pair of CMGs to cancel out gimbal reaction torque [5].

Using CMGs for attitude control becomes feasible after advancement of space technology and construction of bigger spacecrafts. Space stations are the first examples of implementation of CMGs due to their modular structures and large solar panels. In addition to this, the mass of the space stations is distributed and this causes a larger polar moment of inertia values. One solution to control the attitude of the station is using propellant, however, this way is costly and decreases station lifetime depending on resupply missions. Using reaction wheels is another solution; however, CMGs are capable of generating much larger torques on the spacecraft body for limited power and inertia sources [6]. Hence, space stations are one of the most suitable spacecrafts for application of CMGs for attitude control.

Skylab space station was one of the first spacecrafts where CMGs are implemented for attitude control. It had four double gimbal CMGs. Three of them were operational and one of them was for replacement in case of failure of the other three CMGs. CMGs had rotors with 55 cm in diameter and they were spinning around 9000 rpm. The total mass of individual CMGs was 65 kg and they had 3100 N.m.s total angular momentum storage capability. Each unit was able to deliver 160 N.m torque [7]. The designed lifetime of rotor bearing was 10,000 hours and its design started in 1965. When the extended lifetime experiments were conducted, it had been seen that CMGs were able to operate 13,000 hours continuously [8].

Skylab was launched to orbit on May 14th, 1973. One of the CMGs becomes non-operational due to bearing failure after 195 (approximately 4700 hours) days of operation. Moreover, one of the other CMGs showed abnormal conditions but it continued operation. A detailed investigation and study were carried out to find the reason behind the failure and anomalous operation of CMGs. It was found that the reason was improper lubrication of rotor bearings in microgravity environment. The supply oil did not reach bearing contact surfaces. These problems did not emerge during lifetime time tests of CMGs on the ground because Earth's gravitational field helps lubricant to pool and replenish the bearing surfaces [9].

Salyut 3 (or military designation Almaz-2) was in orbit between June 1974 and January 1975 [10]. It was the eastern-bloc space station which contains CMGs [11]. Different from Skylab, these were single gimbal control moment gyroscopes called Gyrodynes. These actuators were also used in MIR space station which is the follow up of Salyut program. A total of 12 Gyrodynes were used on MIR with Kvant 1 and Kvant 2 modules [12]. Each module had six of them with 990 kg total mass [10]. MIR space station was oriented by using Gyrodynes of Kvant 1 module on April 30, 1987. Till the year 1991, four out of six CMGs on Kvant 2 and 1 CMG on Kvant 1 had failed. By July 1992, extra-vehicular activity was required to look at station Gyrodynes. New Gyrodynes were sent to the MIR space station to replace the failed ones on Kvant 2 module on March 1993.

CMGs are also used on International Space Station. These units are double axis CMGs with 4760 N.m.s angular momentum storage capacity and 258 N.m torque output. Four CMGs are mounted on the Truss Z of ISS. During functioning, one of the CMGs failed and its operation has been stopped. Subsequently, another CMG also malfunctioned and it was also taken out of the operations. The reason of failure was detected by onboard sensors. It was found that there was excessive radial acceleration due to unbalance of faulty rotor bearing.

ISS CMGs were returned back to the Earth and possible cause of the errors was investigated with detailed studies. They were returned in 2005 and the root cause was found as loss of preload function which shifts the raceway of bearing balls.

Besides large spacecrafts such as space stations, CMGs are also mounted to satellites. One of the most important mission is BİLSAT for application of CMG technology to mini satellites. BİLSAT is a part of SSTL Disaster Monitoring Constellation and it housed two single axis CMGs in a parallel configuration. These CMGs are capable of applying 100 mN.m torque and they have 0.25 N.m.s angular momentum storage [13]. More recently, all the satellites in CNES high-resolution satellite group (consisting of Pleiades 1A & 1B together with SPOT 6 & SPOT 7) equipped with Airbus D&S 15-45 series CMGs. These actuators can deliver 45 N.m torque and store 15 N.m.s angular momentum. By utilizing four of them, Pleiades 1A was able to perform agile maneuvers up to $3.4\,°/s$ angular velocity. Thanks to this CMGs configuration, the satellite was also capable of taking 30 images of the same location in a single pass [14].

Scaling down of CMGs will probably continue. For instance, a microelectromechanical system (MEMS) CMG with rotary comb drive actuated rotor and parallel plate actuated gimbal was proposed [15]. Different from conventional CMGs, this device is actuated with vibrations, instead of continuous rotations. However, in this study, no detailed simulation results, design or manufacturing details were given. Further research on this idea is done by proposing a MEMS design and

corresponding manufacturing processes. Additional simulation results were also introduced via MEMS simulation software [16]. One novel point stated was the measures taken in order to reduce the effects of disturbances generated by vibratory motions on rotor and gimbal geometry. It was shown that synchronizing an array of such MEMS CMGs with certain phase difference makes possible to cancel vibratory disturbance out.

1.2. Motivation

As it was mentioned above, there are several actuators for attitude control of satellites. Among them, reaction wheels and control moment gyroscopes perform continuous rotations for angular momentum exchange between their rotor masses and spacecraft body. This continuous rotary motion requires bearings and inherently there should be lubrication for the long and safe operation of these rotor bearings. However, lubrication in microgravity environment is a hard topic and its problems do not occur during ground tests of the actuators due to the gravitational field of the Earth. Hence, unexpected actuator failures may occur in orbit and spacecraft becomes useless due to loss of attitude control [17]. It is stated that 83% of the satellite failures in Low Earth Orbit was due to the failure of mechanical bearings [18]. Aforementioned CMG failures were also caused by faulty rotor bearings.

Therefore, in this study, vibratory motion is preferred instead of continuous rotation. Thanks to that, flexible joints may be used to realize the degree of freedom of actuator mechanism instead of revolute joints and mechanical bearings. Hence, there is no need for lubrication and the proposed actuator may have a much longer lifetime.

In the literature, satellite attitude control via vibrations has a small volume. Other than references [15] and [16], there is also a study inspired from the cats which use their tails to orient themselves in the air. The study proposes two masses connected to each other with a ball joint and these masses vibrate to change the structural shape of assembly. Hence, angular momentum is generated on the system of masses [19]. Starting from “single gimbal” vibrating CMG concept, the main contribution of this

study to the literature is developing a mathematical model by using conservation of angular momentum and a better understanding of dynamical characteristics of the concept in more detail via simulation of this model together with two experimental setups for verification. In addition, some improvements and optimization for the performance of this concept have been presented.

CHAPTER 2

MATHEMATICAL MODEL

The starting point of derivations of the mathematical model is a single axis CMG mechanism. The gimbal and rotor geometry of the actuator are excited with sinusoidal position inputs and output of the CMG has been interpreted.

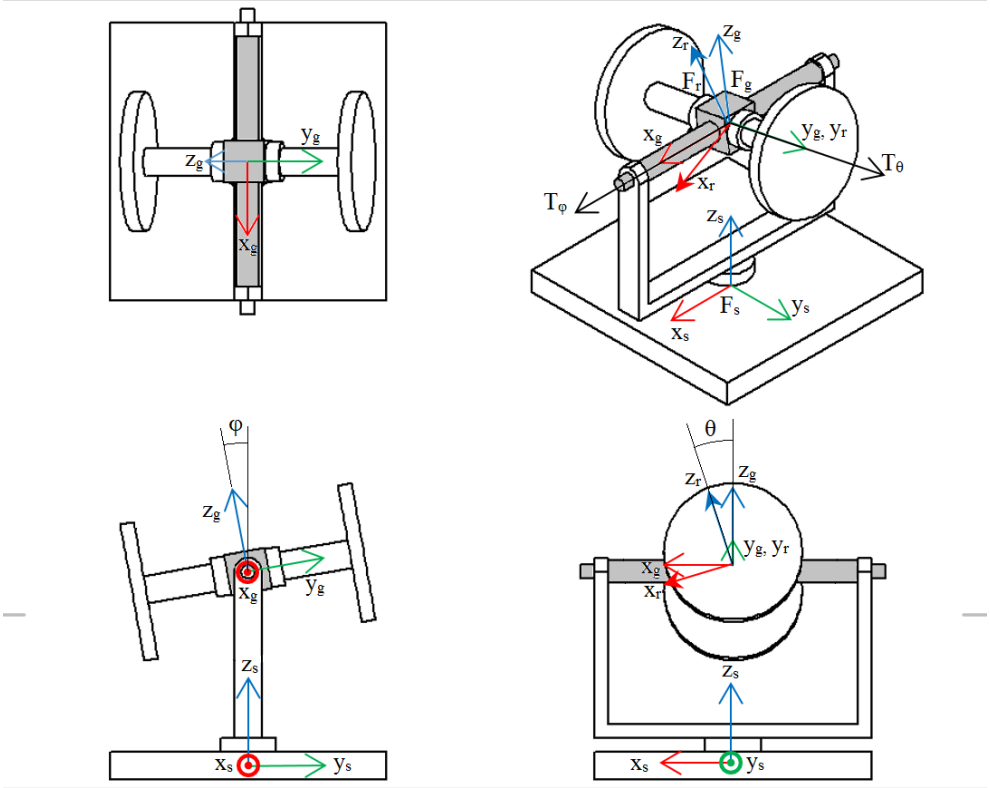

Figure 2.1. Rotor and Gimbal Configuration and Coordinate Systems

The drawing in Figure 2.1 shows the coordinates of the gimbal, rotor and the spacecraft. It is also shown that φ defines the angle of the gimbal axis with respect to spacecraft reference frame and θ is the angle of the rotor axis with respect to the gimbal reference frame.

The mathematical model of the system may be also developed by using Newton-Euler equations. However, these equations give the linear and angular accelerations of the spacecraft body. Hence, numerical integration is required to see the velocity output of the actuator. On the other hand, conservation of angular momentum principle directly gives the angular velocities of the spacecraft body which is the scope of the mathematical model. As a result, a mathematical model of the concept has been derived by using conservation of angular momentum principle. Then, the total angular momentum of the spacecraft and the actuator assembly may be written as,

$$\vec{H}_{total} = \vec{H}_s + \vec{H}_g + \vec{H}_r = \vec{0} \tag{1}$$

$$\vec{H}_s = \check{J}_s \cdot \vec{\omega}_s \qquad \vec{H}_g = \check{J}_g \cdot \vec{\omega}_g \qquad \vec{H}_r = \check{J}_r \cdot \vec{\omega}_r \tag{2}$$

The total angular momentum is taken as zero.

Angular velocity vectors of the gimbal and rotor reference frames are,

$$\vec{\omega}_g = \dot{\phi}\vec{x}_g \qquad \vec{\omega}_r = \dot{\phi}\vec{x}_g + \dot{\theta}\vec{y}_r \tag{3}$$

Inertia dyadics for spacecraft, gimbal and rotor body are represented as,

$$\check{J}_s = J_s^{xx}\vec{x}_s\vec{x}_s + J_s^{yy}\vec{y}_s\vec{y}_s + J_s^{zz}\vec{z}_s\vec{z}_s \tag{4}$$

$$\check{J}_g = J_g^{xx}\vec{x}_g\vec{x}_g + J_g^{yy}\vec{y}_g\vec{y}_g + J_g^{zz}\vec{z}_g\vec{z}_g \tag{5}$$

$$\check{J}_r = J_r^{xx}\vec{x}_r\vec{x}_r + J_r^{yy}\vec{y}_r\vec{y}_r + J_r^{zz}\vec{z}_r\vec{z}_r \tag{6}$$

For simplicity, it is assumed that reference frames are principal reference frames and off-diagonal terms of inertia matrices vanish.

Transformation matrices from the rotor to the gimbal $\hat{C}^{(g/r)}$ and from the gimbal to the spacecraft $\hat{C}^{(s/g)}$ may be shown with following vector algebra:

The rotation of a reference frame A to B can be shown with rotation dyadic as,

$$\vec{u}_k^{(b)} = \check{R}_{ab}\vec{u}_k^{(a)} \tag{7}$$

Where $\vec{u}_k^{(a)}$ is k[th] unit vector of reference frame A and $\vec{u}_k^{(b)}$ is k[th] unit vector of reference frame B. $\check{R}_{ab}$ is rotation dyadic from frame A to B. This vector equation can be represented in any frame. For mathematical simplicity, it is represented in frame A.

$$\bar{u}_k^{(b/a)} = \hat{R}_{ab}^{(a)} \bar{u}_k^{(a/a)} \tag{8}$$

$\bar{u}_k^{(a/a)}$ means that unit vectors of frame A is represented again in frame A and this gives unit column matrix representation of unit vectors. They are given in the notation as,

$$\bar{u}_k^{(a/a)} = \bar{u}_k \tag{9}$$

$$\bar{u}_1 = \begin{bmatrix} 1 \\ 0 \\ 0 \end{bmatrix} \quad \bar{u}_2 = \begin{bmatrix} 0 \\ 1 \\ 0 \end{bmatrix} \quad \bar{u}_3 = \begin{bmatrix} 0 \\ 0 \\ 1 \end{bmatrix} \tag{10}$$

However $\bar{u}_k^{(b/a)}$ shows the representation of unit vectors of frame B in frame A and transformation matrix is needed for calculation.

$$\bar{u}_k^{(b/a)} = \hat{C}^{(a/b)} \bar{u}_k^{(b/b)} = \hat{C}^{(a/b)} \bar{u}_k \tag{11}$$

where $\hat{C}^{(a/b)}$ is the transformation matrix from frame B to A.

Putting into Eq. (8) gives,

$$\hat{C}^{(a/b)} \bar{u}_k^{(b/b)} = \hat{R}_{ab}^{(a)} \bar{u}_k^{(a/a)} \tag{12}$$

$$\hat{C}^{(a/b)} \bar{u}_k = \hat{R}_{ab}^{(a)} \bar{u}_k \tag{13}$$

$$\hat{C}^{(a/b)} = \hat{R}_{ab}^{(a)} \tag{14}$$

Hence, transformation matrix from frame B to A is equal to rotation matrix from frame A to B.

Rotation matrices from spacecraft to gimbal $\hat{R}_{sg}$ and, from gimbal to rotor $\hat{R}_{gr}$ are defined in spacecraft and gimbal reference frames respectively and, they are written in exponential form as,

$$\hat{R}_{sg}^{(s)} = e^{\tilde{x}\varphi} \qquad \hat{R}_{gr}^{(g)} = e^{\tilde{y}\theta} \tag{15}$$

(~) symbol over unit vectors means that cross product matrix form of unit vectors is represented. For example,

$$\tilde{x} = \begin{bmatrix} 0 & -x_3 & x_2 \\ x_3 & 0 & -x_1 \\ -x_2 & x_1 & 0 \end{bmatrix} \tag{16}$$

According to Eq. (14) transformation matrices are,

$$\hat{C}^{(s/g)} = \hat{R}_{sg}^{(s)} = e^{\tilde{x}\varphi} \tag{17}$$

$$\hat{C}^{(g/r)} = \hat{R}_{gr}^{(g)} = e^{\tilde{y}\theta} \tag{18}$$

The inverse of rotation and transformation matrices are,

$$\hat{C}^{(g/s)} = \hat{R}_{gs}^{(s)} = e^{-\tilde{x}\varphi} \tag{19}$$

$$\hat{C}^{(r/g)} = \hat{R}_{rg}^{(g)} = e^{-\tilde{y}\theta} \tag{20}$$

Now angular momentum vector of gimbal body can be represented at gimbal reference frame as follows,

$$\vec{H}_g = \check{J}_g \vec{\omega}_g = (J_g^{xx}\vec{x}_g\vec{x}_g + J_g^{yy}\vec{y}_g\vec{y}_g + J_g^{zz}\vec{z}_g\vec{z}_g) \cdot \dot{\varphi}\vec{x}_g = J_g^{xx}\dot{\varphi}\vec{x}_g \tag{21}$$

$$\bar{H}_g^{(g)} = J_g^{xx}\dot{\varphi}\bar{x} \tag{22}$$

In the same manner, the angular momentum of the rotor body is written in its own reference frame and then transformed to the gimbal reference frame as follows,

$$\vec{H}_r = \check{J}_r \vec{\omega}_r = (J_r^{xx}\vec{x}_r\vec{x}_r + J_r^{yy}\vec{y}_r\vec{y}_r + J_r^{zz}\vec{z}_r\vec{z}_r) \cdot (\dot{\varphi}\vec{x}_g + \dot{\theta}\vec{y}_r) \tag{23}$$

When Eq. (23) is resolved in rotor reference frame,

$$\bar{H}_r^{(r)} = (J_r^{xx}\bar{x}\bar{x} + J_r^{yy}\bar{y}\bar{y} + J_r^{zz}\bar{z}\bar{z}) \cdot (\dot{\varphi}C^{(r/g)}\bar{x} + \dot{\theta}\bar{y}) \tag{24}$$

$$\bar{H}_r^{(r)} = (J_r^{xx}\bar{x}\bar{x} + J_r^{yy}\bar{y}\bar{y} + J_r^{zz}\bar{z}\bar{z}) \cdot (\dot{\varphi}e^{-\tilde{y}\theta}\bar{x} + \dot{\theta}\bar{y}) \tag{25}$$

$$\bar{H}_r^{(r)} = (J_r^{xx}\bar{x}\bar{x} + J_r^{yy}\bar{y}\bar{y} + J_r^{zz}\bar{z}\bar{z}) \cdot (\dot{\varphi}(\bar{x}\cos\theta + \bar{z}\sin\theta) + \dot{\theta}\bar{y}) \tag{26}$$

$$\bar{H}_r^{(r)} = J_r^{xx}\dot{\varphi}\cos\theta\,\bar{x} + J_r^{yy}\dot{\theta}\bar{y} + J_r^{zz}\dot{\varphi}\sin\theta\,\bar{z} \tag{27}$$

Finally,

$$\vec{H}_r = J_r^{xx}\dot{\varphi}\cos\theta\,\vec{x}_r + J_r^{yy}\dot{\theta}\vec{y}_r + J_r^{zz}\dot{\varphi}\sin\theta\vec{z}_r \tag{28}$$

However, in order to add scalar components of two vectors, they must be resolved in the same reference frame. Then, Eq. (28) transforms to gimbal reference frame as

$$\bar{H}_r^{(g)} = J_r^{xx}\dot{\varphi}\cos\theta\,\bar{x}_{(r/g)} + J_r^{yy}\dot{\theta}\bar{y}_{(r/g)} + J_r^{zz}\dot{\varphi}\sin\theta\bar{z}_{(r/g)} \tag{29}$$

$$\bar{H}_r^{(g)} = J_r^{xx}\dot{\varphi}\cos\theta\,\hat{C}^{(g/r)}\bar{x} + J_r^{yy}\dot{\theta}\hat{C}^{(g/r)}\bar{y} + J_r^{zz}\dot{\varphi}\sin\theta\hat{C}^{(g/r)}\bar{z} \tag{30}$$

$$\bar{H}_r^{(g)} = J_r^{xx}\dot{\varphi}\cos\theta\,e^{\tilde{y}\theta}\bar{x} + J_r^{yy}\dot{\theta}e^{\tilde{y}\theta}\bar{y} + J_r^{zz}\dot{\varphi}\sin\theta e^{\tilde{y}\theta}\bar{z} \tag{31}$$

$$\bar{H}_r^{(g)} = J_r^{xx}\dot{\varphi}\cos\theta\,(\bar{x}\cos\theta - \bar{z}\sin\theta) + J_r^{yy}\dot{\theta}\bar{y} + J_r^{zz}\dot{\varphi}\sin\theta\,(\bar{z}\cos\theta + \bar{x}\sin\theta) \tag{32}$$

Collecting terms,

$$\bar{H}_r^{(g)} = [J_r^{xx}\dot{\varphi}\,(\cos\theta)^2 + J_r^{zz}\dot{\varphi}(\sin\theta)^2]\bar{x} + J_r^{yy}\dot{\theta}\bar{y} + [J_r^{zz}\dot{\varphi}\sin\theta\cos\theta - J_r^{xx}\dot{\varphi}\sin\theta\cos\theta]\bar{z} \tag{33}$$

Hence angular momentum of the rotor body can be represented by gimbal reference frame unit vectors as,

$$\vec{H}_r = [J_r^{xx}\dot{\varphi}\,(\cos\theta)^2 + J_r^{zz}\dot{\varphi}(\sin\theta)^2]\vec{x}_g + J_r^{yy}\dot{\theta}\vec{y}_g + [J_r^{zz}\dot{\varphi}\sin\theta\cos\theta - J_r^{xx}\dot{\varphi}\sin\theta\cos\theta]\vec{z}_g \tag{34}$$

The angular momentum of the spacecraft body is,

$$\vec{H}_s = -\vec{H}_g - \vec{H}_r \tag{35}$$

$$\vec{H}_s = -\big[J_r^{xx}\dot{\varphi}\,(\cos\theta)^2 + J_r^{zz}\dot{\varphi}(\sin\theta)^2 + J_g^{xx}\dot{\varphi}\big]\vec{x}_g - J_r^{yy}\dot{\theta}\vec{y}_g - [(J_r^{zz} - J_r^{xx})\dot{\varphi}\sin\theta\cos\theta]\vec{z}_g \tag{36}$$

Angular momentum vector of spacecraft body may be represented at spacecraft reference frame for further investigation.

$$\bar{H}_s^{(s)} = -\big[J_r^{xx}\dot{\varphi}\,(\cos\theta)^2 + J_r^{zz}\dot{\varphi}(\sin\theta)^2 + J_g^{xx}\dot{\varphi}\big]\bar{x}_{(g/s)} - J_r^{yy}\dot{\theta}\bar{y}_{(g/s)} - [(J_r^{zz} - J_r^{xx})\dot{\varphi}\sin\theta\cos\theta]\bar{z}_{(g/s)} \tag{37}$$

$$\bar{H}_s^{(s)} = -\left[J_r^{xx}\dot{\varphi}\,(\cos\theta)^2 + J_r^{zz}\dot{\varphi}(\sin\theta)^2 + J_g^{xx}\dot{\varphi}\right]\hat{C}^{(s/g)}\bar{x} - J_r^{yy}\dot{\theta}\hat{C}^{(s/g)}\bar{y} - [(J_r^{zz} - J_r^{xx})\dot{\varphi}\sin\theta\cos\theta]\hat{C}^{(s/g)}\bar{z} \quad (38)$$

$$\bar{H}_s^{(s)} = -\left[J_r^{xx}\dot{\varphi}\,(\cos\theta)^2 + J_r^{zz}\dot{\varphi}(\sin\theta)^2 + J_g^{xx}\dot{\varphi}\right]e^{\tilde{x}\varphi}\bar{x} - J_r^{yy}\dot{\theta}e^{\tilde{x}\varphi}\bar{y} - [(J_r^{zz} - J_r^{xx})\dot{\varphi}\sin\theta\cos\theta]e^{\tilde{x}\varphi}\bar{z} \quad (39)$$

$$\bar{H}_s^{(s)} = -\left[J_r^{xx}\dot{\varphi}\,(\cos\theta)^2 + J_r^{zz}\dot{\varphi}(\sin\theta)^2 + J_g^{xx}\dot{\varphi}\right]\bar{x} - J_r^{yy}\dot{\theta}(\bar{y}\cos\varphi + \bar{z}\sin\varphi) - [(J_r^{zz} - J_r^{xx})\dot{\varphi}\sin\theta\cos\theta](\bar{z}\cos\varphi - \bar{y}\sin\varphi) \quad (40)$$

Collecting terms yields,

$$\bar{H}_s^{(s)} = -\left[J_r^{xx}\dot{\varphi}\,(\cos\theta)^2 + J_r^{zz}\dot{\varphi}(\sin\theta)^2 + J_g^{xx}\dot{\varphi}\right]\bar{x} - \left[J_r^{yy}\dot{\theta}\cos\varphi - (J_r^{zz} - J_r^{xx})\dot{\varphi}\cos\theta\sin\theta\sin\varphi\right]\bar{y} - \left[J_r^{yy}\dot{\theta}\sin\varphi + (J_r^{zz} - J_r^{xx})\dot{\varphi}\cos\theta\sin\theta\cos\varphi\right]\bar{z} \quad (41)$$

Finally, the vector equation of spacecraft angular momentum in terms of unit vectors of spacecraft reference frame is,

$$\vec{H}_s = -\left[J_r^{xx}\dot{\varphi}\,(\cos\theta)^2 + J_r^{zz}\dot{\varphi}(\sin\theta)^2 + J_g^{xx}\dot{\varphi}\right]\vec{x}_s - \left[J_r^{yy}\dot{\theta}\cos\varphi - (J_r^{zz} - J_r^{xx})\dot{\varphi}\cos\theta\sin\theta\sin\varphi\right]\vec{y}_s - \left[J_r^{yy}\dot{\theta}\sin\varphi + (J_r^{zz} - J_r^{xx})\dot{\varphi}\cos\theta\sin\theta\cos\varphi\right]\vec{z}_s \quad (42)$$

Where,

$$\varphi = \varphi_0\sin(2\pi ft) \quad \theta = \theta_0\sin(2\pi ft + \beta) \quad (43)$$

$$\dot{\varphi} = 2\pi f\varphi_0\cos(2\pi ft) \quad \dot{\theta} = 2\pi f\theta_0\cos(2\pi ft + \beta) \quad (44)$$

are the input position and velocities of gimbal and rotor bodies and, β angle shows the input phase difference between rotor and gimbal axes.

Scalar angular velocity output equations can be obtained as follows:

$$\vec{H}_s = \vec{J}_s\vec{\omega}_s = (J_s^{xx}\vec{x}_s\vec{x}_s + J_s^{yy}\vec{y}_s\vec{y}_s + J_s^{zz}\vec{z}_s\vec{z}_s)\cdot(\omega_{sx}\vec{x}_s + \omega_{sy}\vec{y}_s + \omega_{sz}\vec{z}_s) \quad (45)$$

$$\vec{H}_s = J_s^{xx}\omega_{sx}\vec{x}_s + J_s^{yy}\omega_{sy}\vec{y}_s + J_s^{zz}\omega_{sz}\vec{z}_s \quad (46)$$

Equating coefficients of Eq. (42) and Eq. (46), scalar angular velocity equations of spacecraft are obtained.

$$\omega_{sx} = -\frac{1}{J_s^{xx}}\left[J_r^{xx}\dot{\varphi}\,(\cos\theta)^2 + J_r^{zz}\dot{\varphi}(\sin\theta)^2 + J_g^{xx}\dot{\varphi}\right] \quad (47)$$

$$\omega_{sy} = -\frac{1}{J_s^{yy}}\left[J_r^{yy}\dot{\theta}\cos\varphi - (J_r^{zz} - J_r^{xx})\dot{\varphi}\cos\theta\sin\theta\sin\varphi\right] \quad (48)$$

$$\omega_{sz} = -\frac{1}{J_s^{zz}}\left[J_r^{yy}\dot{\theta}\sin\varphi + (J_r^{zz} - J_r^{xx})\dot{\varphi}\cos\theta\sin\theta\cos\varphi\right] \quad (49)$$

The desired output of the CMG is ω_{sz} and when inputs are given to Eq. (49),

$$\begin{aligned}\omega_{sz} = -\frac{1}{J_s^{zz}}\big[&J_r^{yy}\theta_0 2\pi f\sin(\varphi_0\sin(2\pi ft))\cos(2\pi ft+\beta) + (J_r^{zz}\\ &- J_r^{xx})\varphi_0\,2\pi f\cos(\varphi_0\sin(2\pi ft))\sin(\theta_0\sin(2\pi ft\\ &+\beta))\cos(\theta_0\sin(2\pi ft+\beta))\cos(2\pi ft)\big]\end{aligned} \quad (50)$$

The torques on the spacecraft body may also be derived by taking derivative of the angular momentum vector with respect to inertial reference frame. According to Coriolis' Transport theorem,

$$D_0\vec{H}_s = D_s\vec{H}_s + \vec{\omega}_s \times \vec{H}_s \quad (51)$$

Cross product of the angular velocity of spacecraft and angular momentum of spacecraft is zero. Because two vectors are parallel. Hence,

$$D_0\vec{H}_s = D_s\vec{H}_s \quad (52)$$

The components of the angular momentum vector have already been calculated and its derivative with respect to spacecraft reference frame is just the derivatives of the components.

$$
\begin{aligned}
D_0\vec{H}_s = \Big[& J_r^{xx}\left(\ddot{\varphi}(\cos\theta)^2 - 2\dot{\varphi}\dot{\theta}\cos\theta\sin\theta\right) \\
& + J_r^{zz}\left(\ddot{\varphi}(\sin\theta)^2 + 2\dot{\varphi}\dot{\theta}\cos\theta\sin\theta\right) + J_g^{xx}\ddot{\varphi}\Big]\vec{x}_s \\
& + \Big[J_r^{yy}\left(\ddot{\theta}\cos\varphi - \dot{\theta}\dot{\varphi}\sin\varphi\right) - (J_r^{zz} \\
& - J_r^{xx})(\ddot{\varphi}\cos\theta\sin\theta\sin\varphi - \dot{\varphi}\dot{\theta}(\sin\theta)^2\sin\varphi \\
& + \dot{\varphi}\dot{\theta}(\cos\theta)^2\sin\varphi + \dot{\varphi}^2\cos\theta\sin\theta\cos\varphi)\Big]\vec{y}_s \\
& + \Big[J_r^{yy}\left(\ddot{\theta}\sin\varphi + \dot{\varphi}\dot{\theta}\cos\varphi\right) + (J_r^{zz} \\
& - J_r^{xx})(\ddot{\varphi}\cos\theta\sin\theta\cos\varphi - \dot{\varphi}\dot{\theta}(\sin\theta)^2\cos\varphi \\
& + \dot{\varphi}\dot{\theta}(\cos\theta)^2\cos\varphi - \dot{\varphi}^2\cos\theta\sin\theta\cos\varphi)\Big]\vec{z}_s
\end{aligned}
\tag{53}
$$

CHAPTER 3

EFFECT OF EXCITATION PARAMETERS

It is not very intuitive to grasp the dynamical characteristics of the output angular velocity from analytical expression in Eq. (50). Hence, the effect of system excitation parameters such as phase difference between the rotor and gimbal excitation axes, excitation frequency, and excitation amplitudes was investigated to gain insight about output behavior of the actuator. Output velocity graphs for desired rotation axes were obtained and interpreted. For geometry at Figure 2.1, the aluminum material is used for all solid bodies and hypothetical inertia values were obtained as:

$$J_r = \begin{bmatrix} 1.024492E-04 & 0 & 0 \\ 0 & 1.705278E-05 & 0 \\ 0 & 0 & 1.024492E-04 \end{bmatrix} kg.m^2$$

$$J_g = \begin{bmatrix} 4.163880E-07 & 0 & 0 \\ 0 & 1.140054E-05 & 0 \\ 0 & 0 & 1.140054E-05 \end{bmatrix} kg.m^2$$

$$J_s = \begin{bmatrix} 6.564948E-04 & 0 & 0 \\ 0 & 6.564948E-04 & 0 \\ 0 & 0 & 6.564948E-04 \end{bmatrix} kg.m^2$$

for rotor, gimbal, and spacecraft, respectively. Rotor geometry is axisymmetric and spacecraft is assumed as a uniform solid cube.

The angular velocity output on Z axis of spacecraft reference frame in Eq. (50) may be simplified by assuming the amplitude of vibrations is small. Hence, the angular velocity output becomes,

$$\omega_{sz} \cong -\frac{1}{J_s^{zz}}\left[J_r^{yy}\theta_0 2\pi f\varphi_0 \sin(2\pi ft)\cos(2\pi ft+\beta) + (J_r^{zz} - J_r^{xx})\varphi_0 2\pi f\theta_0 \sin(2\pi ft+\beta)\cos(2\pi ft)\right] \tag{54}$$

Collecting terms yield,

$$\omega_{sz} \cong -\frac{\theta_0\varphi_0 2\pi f}{J_s^{zz}}\left[J_r^{yy} \sin(2\pi ft)\cos(2\pi ft+\beta) + (J_r^{zz} - J_r^{xx})\sin(2\pi ft+\beta)\cos(2\pi ft)\right] \tag{55}$$

The angular velocity output may also be represented with following mathematical manipulations,

$$\begin{aligned}\omega_{sz} \cong -\frac{\theta_0\varphi_0 2\pi f}{J_s^{zz}}\Bigg[&\frac{J_r^{yy}+J_r^{zz}-J_r^{xx}}{2}\sin(2\pi ft)\cos(2\pi ft+\beta)\\ &+\frac{J_r^{yy}-J_r^{zz}+J_r^{xx}}{2}\sin(2\pi ft)\cos(2\pi ft+\beta)\\ &+\frac{J_r^{yy}+J_r^{zz}-J_r^{xx}}{2}\sin(2\pi ft+\beta)\cos(2\pi ft)\\ &-\frac{J_r^{yy}-J_r^{zz}+J_r^{xx}}{2}\sin(2\pi ft+\beta)\cos(2\pi ft)\Bigg]\end{aligned} \tag{56}$$

Using sine summation formulas yield,

$$\omega_{sz} \cong -\frac{\theta_0\varphi_0 2\pi f}{J_s^{zz}}\left[\frac{J_r^{yy}+J_r^{zz}-J_r^{xx}}{2}\sin(4\pi ft+\beta) - \frac{J_r^{yy}-J_r^{zz}+J_r^{xx}}{2}\sin\beta\right] \tag{57}$$

The Eq. (57) approximately represents the angular velocity gain of spacecraft. The expression inside square brackets in Eq. (57) shows the trend of the velocity curve and the coefficient before the square bracket includes excitation frequency f and

excitation amplitudes θ_0 and φ_0. The first expression inside square bracket is the oscillating term of the angular velocity gain and the second term is the mean angular velocity term of the angular velocity gain. This means that, spacecraft angular velocity oscillates at twice the excitation frequency and it has a mean value depending on phase difference given between rotor and gimbal excitations.

3.1. Phase Difference

In that simulation, rotor and gimbal axes are excited with 1 Hz sinusoidal position inputs with 5 degrees amplitude. Excitation amplitudes start from 0° and increase up to 5° in 2 seconds in order to eliminate initial condition effects on the system due to sudden excitation of the torques on rotor and gimbal axes. According to inertia values given above, angular velocity gain for 0° and 90° phase difference was plotted.

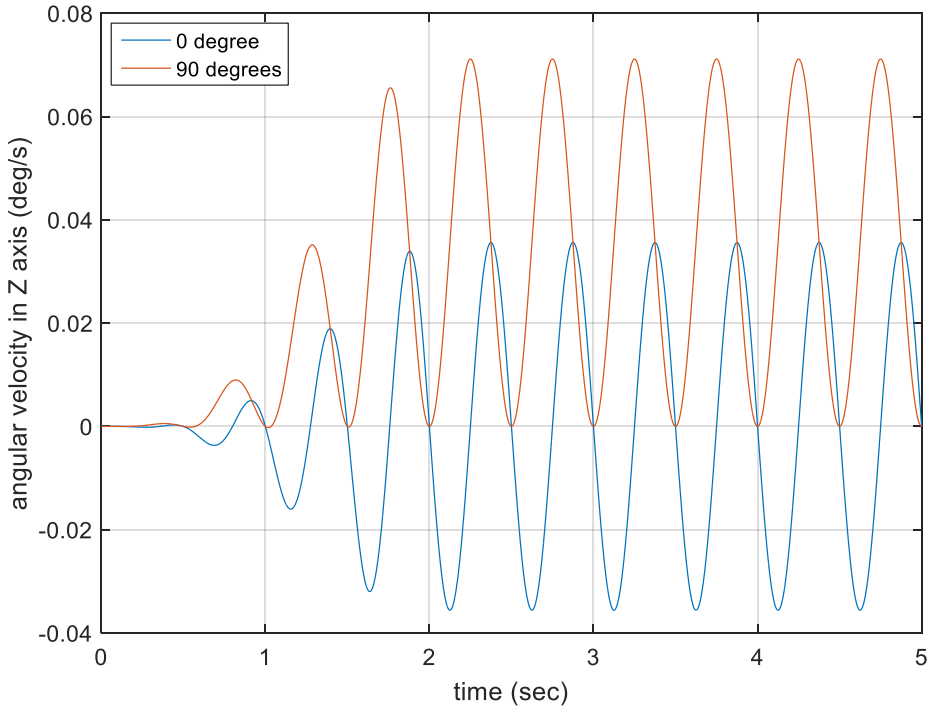

Figure 3.1. Angular velocity gain on spacecraft reference frame for 0° and 90° phase difference

It may be seen from Figure 3.1 that there is a difference between the net angular velocity gains for 0º and 90º phase difference between rotor and gimbal axes. For 0º phase difference, spacecraft simply vibrates at its original orientation and there is no net angular velocity on desired spacecraft rotation axis. However, if 90º phase difference is given, a net angular velocity is obtained.

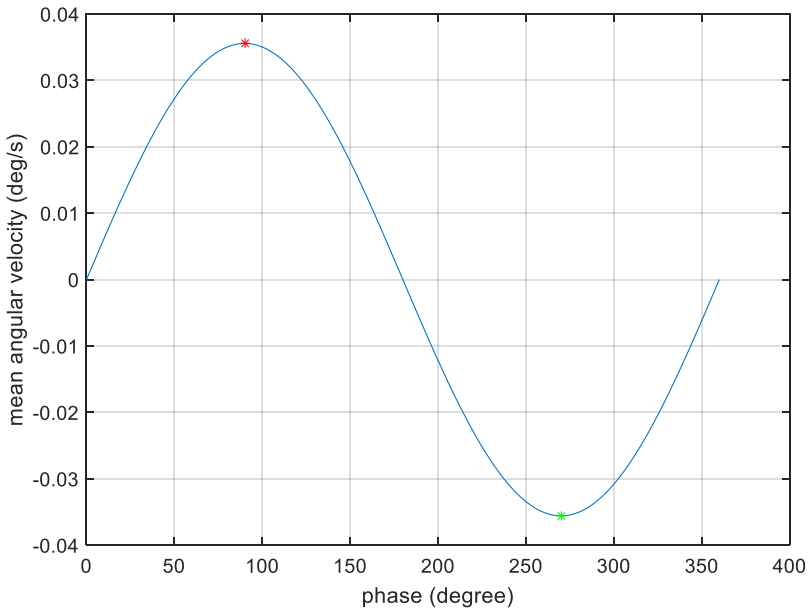

Figure 3.2. Phase difference vs mean angular velocity gain

For detailed interpretation, the phase difference versus mean angular velocity gain graph was obtained (Figure 3.2). Mean angular velocity is calculated as an average value of the induced velocity. There are three outcomes from this simulation.

- First, there is no net angular velocity on spacecraft useful rotation axis if the phase difference between rotor and gimbal axes is 0º, 180º and 360º.
- Second, maximum angular velocity is obtained at 90º and 270º phase differences.
- Third, both angular velocity output magnitude and direction can be controlled by changing the phase difference between rotor and gimbal axes from -90º to +90º.

It may directly be seen from Eq. (57) that phase difference contributes the mean angular velocity term with $\sin\beta$. Hence, above numerical results in Figure 3.2 shows a very close trend to sine curve as presented second term inside the square brackets of Eq. (57).

3.2. Frequency

As it is mentioned before, if small angles are assumed for excitation, the angular velocity equation reduced to Eq. (57). Hence, it may be observed from Eq. (57) that there is a proportional relation between excitation frequency and the angular velocity. If excitation frequencies are doubled for rotor and gimbal axes, output mean and maximum angular velocity are also doubled. This means that the actuator shows better performance with higher excitation frequencies. The phase difference is 90° for both results. The frequency of output angular velocity is two times of excitation frequencies.

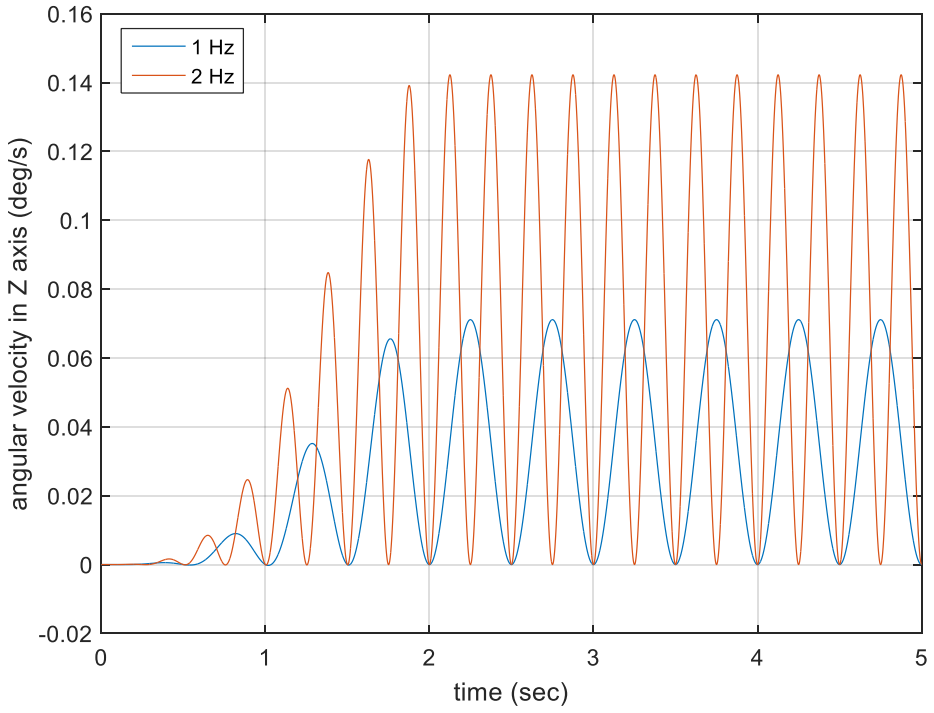

Figure 3.3. Effect of excitation frequency on angular velocity output

3.3. Amplitude

When Eq. (57) is investigated, there is a quadratic relation between excitation amplitudes and angular velocity if amplitudes θ_0 and φ_0 are equal to each other. When excitation amplitudes are doubled, angular velocity output is multiplied by four. Phase difference is 90° for both results. Increasing excitation amplitudes also increases the magnitude output angular velocity.

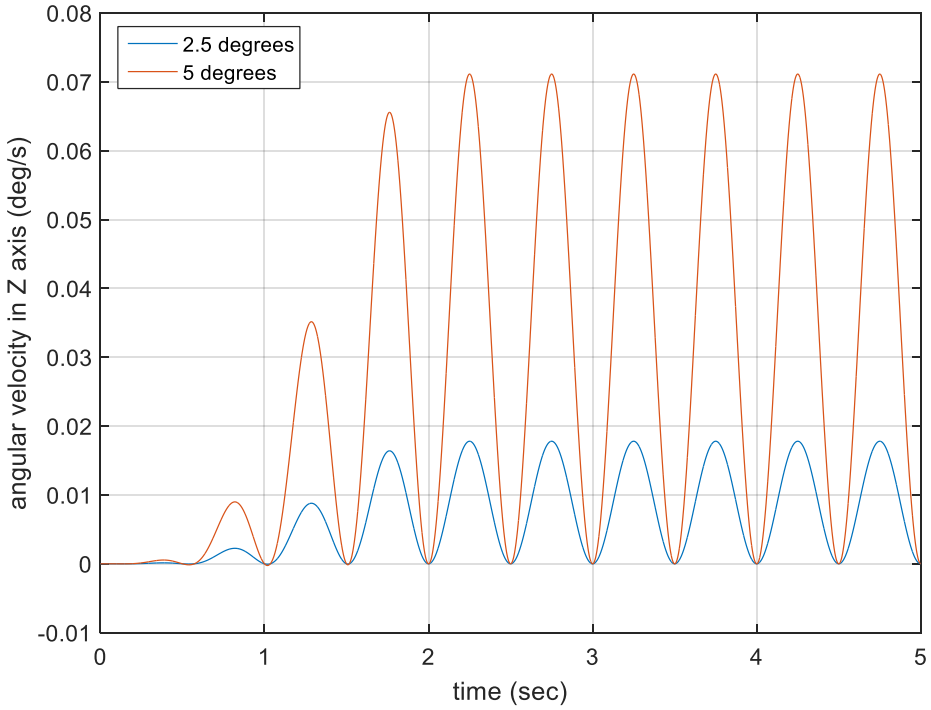

Figure 3.4. Effect of excitation amplitude on angular velocity output

CHAPTER 4

STABILIZATION AND OPTIMIZATION OF THE ACTUATOR

4.1. Cancellation of Vibrations on Rotor and Gimbal Axes

The angular velocity output for all three axes of the spacecraft reference frame may be seen in Figure 4.1. Due to excitations on rotor and gimbal axes, there occur reaction vibrations on the spacecraft body. When these responses are compared to output angular velocity on the desired rotation axis, it has been seen that the amplitude of reaction vibrations are very large with respect to the amplitude of output angular velocity. In order to cancel out these unwanted vibrations, a pair of CMGs may be used.

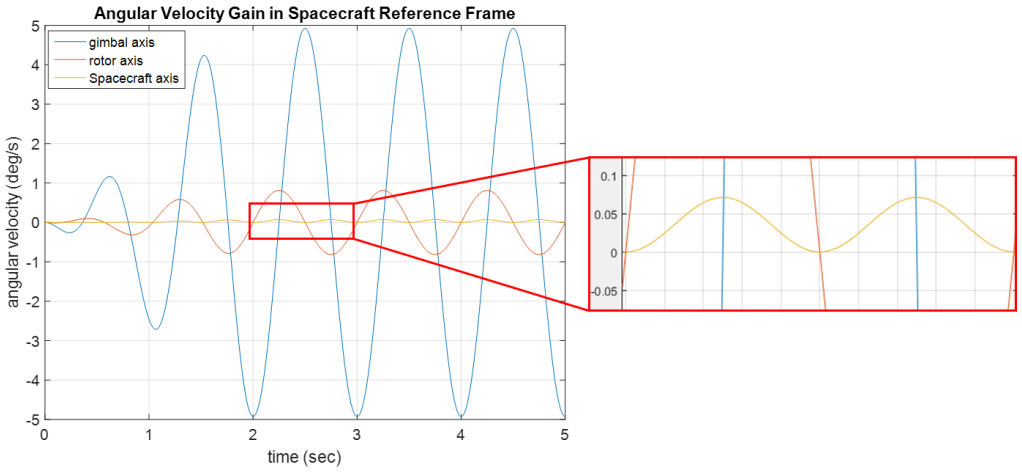

Figure 4.1. Angular velocity output for all three axes of spacecraft reference frame

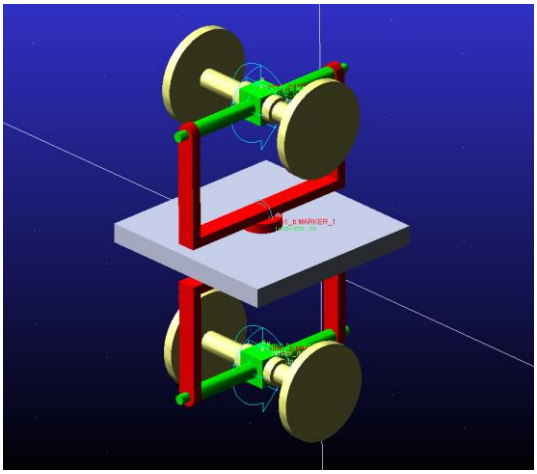

Figure 4.2. Pair of CMGs to cancel out excitation vibrations on the spacecraft body

In the configuration presented in Figure 4.2, CMGs are identical. The upper and lower CMGs move out of phase to cancel out excitation vibrations on rotor and gimbal axes. The individual CMGs have 90º phase difference between their own rotor and gimbal axes. In Figure 4.3, results are presented for 1 Hz excitations with 5º amplitude. As can be seen from Figure 4.3, X and Y axis vibrations are totally canceled out. Output angular velocity is also increased with respect to single CMG's performance. However, as can be seen from Figure 4.3, output angular velocity (green plot) also has vibratory nature and this oscillating angular velocity profile will not be suitable for optical devices during operation, dropping the image quality. Smooth operation and rotation of spacecraft are critical for such purposes. In the following part, the method developed to eliminate these oscillations on angular velocity output is proposed.

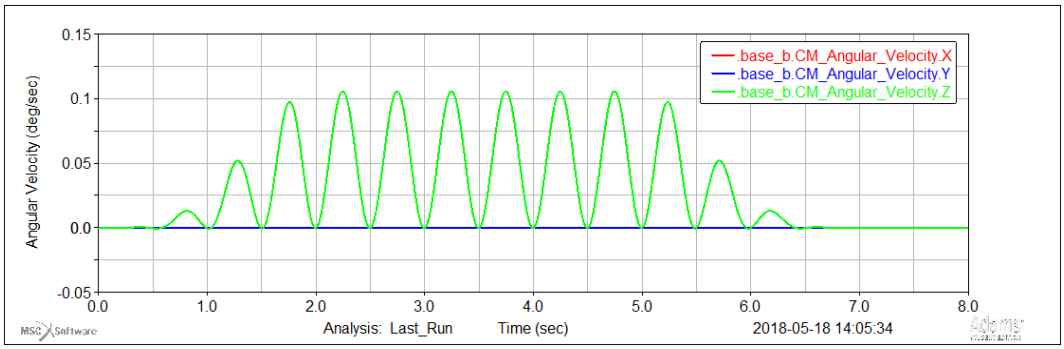

Figure 4.3. Angular velocity output of the pair of CMGs in ADAMS

4.2. Cancellation of Vibrations on Desired Rotation Axis

In the previous part, it was shown that there is vibration in the output axis of the CMG and consequently on spacecraft. The reason behind this oscillation is using axisymmetric rotor geometry such as a cylinder, cube or sphere. During numerical simulations with arbitrary inertia values, it has been observed that oscillations on angular velocity output may change with inertia distribution and there may be optimum inertia distribution to minimize this unwanted oscillation on angular velocity output. Large oscillatory motions are also present in the other two axis as well, due to excitation response torques. However, it was shown that by using a pair of CMGs with out of phase excitations, those oscillations in the remaining axis may be nulled (Figure 4.3). On the other hand, oscillations on the angular velocity output on the spacecraft rotation axis (Z axis) remains. In this part, a mathematical approach to find optimum rotor geometry has been proposed.

4.2.1. Optimum Inertia Distribution of Rotor Geometry

Mathematical proof of optimum rotor inertia distribution was derived from the scalar Z-axis angular velocity output of the actuator. To simplify the analysis, the phase difference β, is taken as zero. Then, the spacecraft z-axis angular velocity expression simplifies to,

$$\begin{aligned}&\omega_{sz}\\&= -\frac{1}{J_s^{zz}}\left[J_r^{yy}\theta_0 2\pi f \sin(\varphi_0 \sin(2\pi f t))\cos(2\pi f t) + (J_r^{zz}\right.\\&\left.- J_r^{xx})\varphi_0\, 2\pi f \cos(\varphi_0 \sin(2\pi f t))\sin(\theta_0 \sin(2\pi f t))\cos(\theta_0 \sin(2\pi f t))\cos(2\pi f t)\right]\end{aligned} \tag{58}$$

It was previously shown that when there is no phase difference, there is no net useful rotation but spacecraft vibrates around its original position (Figure 3.1). When there are no angular oscillations and no net angular velocity, ω_{sz} must be zero. Then,

$$\begin{aligned}&J_r^{yy}\theta_0 2\pi f \sin(\varphi_0 \sin(2\pi f t))\cos(2\pi f t)\\&+ (J_r^{zz} - J_r^{xx})\varphi_0 2\pi f \cos(\varphi_0 \sin(2\pi f t))\sin(\theta_0 \sin(2\pi f t))\cos(\theta_0 \sin(2\pi f t))\cos(2\pi f t)\\&= 0\end{aligned} \tag{59}$$

Collecting inertia terms on the left-hand side yields,

$$\frac{J_r^{yy}}{J_r^{xx}-J_r^{zz}} = \frac{\varphi_0 2\pi f \cos(\varphi_0 \sin(2\pi ft)) \sin(\theta_0 \sin(2\pi ft)) \cos(\theta_0 \sin(2\pi ft)) \cos(2\pi ft)}{\theta_0 2\pi f \sin(\varphi_0 \sin(2\pi ft)) \cos(2\pi ft)} \tag{60}$$

Canceling out terms gives,

$$\frac{J_r^{yy}}{J_r^{xx}-J_r^{zz}} = \frac{\varphi_0 \cos(\varphi_0 \sin(2\pi ft)) \sin(\theta_0 \sin(2\pi ft)) \cos(\theta_0 \sin(2\pi ft))}{\theta_0 \sin(\varphi_0 \sin(2\pi ft))} \tag{61}$$

Eq. (60) may be further simplified assuming that oscillation amplitudes of gimbal and rotor axis (φ_0 and θ_0) are small and equal each other,

$$\frac{J_r^{yy}}{J_r^{xx}-J_r^{zz}} = \cos(\varphi_0 \sin(2\pi ft))^2 \cong 1 \tag{62}$$

$$J_r^{yy} + J_r^{zz} \cong J_r^{xx} \tag{63}$$

Eq. (63) shows the optimum distribution of rotor inertia values to minimize oscillations on angular velocity output of the actuator. This result is the novel part of this thesis.

The Eq. (63) may also be obtained by equating oscillating term of Eq. (57) to zero.

$$\frac{J_r^{yy} + J_r^{zz} - J_r^{xx}}{2} \sin(4\pi ft + \beta) = 0 \tag{64}$$

$$J_r^{yy} + J_r^{zz} - J_r^{xx} = 0 \tag{65}$$

$$J_r^{yy} + J_r^{zz} = J_r^{xx} \tag{66}$$

4.2.2. Simplified Angular Velocity Equation

By putting Eq. (63) into Eq. (50), a simple angular velocity output equation can be obtained. After inserting angular Eq. (50) becomes,

$$\omega_{sz} = -\frac{J_r^{yy}}{J_s^{zz}}[\theta_0 2\pi f\, sin(\varphi_0\, sin(2\pi ft))\, cos(2\pi ft+\beta) - \varphi_0\, 2\pi f cos(\varphi_0\, sin(2\pi ft))\, sin(\theta_0\, sin(2\pi ft + \beta))\, cos(\theta_0\, sin(2\pi ft+\beta))\, cos(2\pi ft)] \quad (67)$$

Small angle assumption for φ_0 and θ_0 gives,

$$\omega_{sz} \cong -\frac{J_r^{yy}}{J_s^{zz}} 2\pi f[\theta_0\varphi_0\, sin(2\pi ft)\, cos(2\pi ft+\beta) - \varphi_0\theta_0\, sin(2\pi ft+\beta)\, cos(2\pi ft)] \quad (68)$$

Then, trigonometric identity was used below to simplify the Eq. (50) even more,

$$sin(\alpha-\gamma) = sin\,\alpha\, cos\,\gamma - sin\,\gamma\, cos\,\alpha \quad where \quad \alpha = 2\pi ft \;\; and \;\; \gamma = 2\pi ft+\beta \quad (69)$$

$$\omega_{sz} \cong -\frac{J_r^{yy}}{J_s^{zz}}\theta_0\varphi_0 2\pi f\, sin(2\pi ft - 2\pi ft - \beta) \quad (70)$$

$$\omega_{sz} \cong \frac{J_r^{yy}}{J_s^{zz}}\theta_0\varphi_0 2\pi f\, sin\,\beta \quad (71)$$

The Eq. (71) may also be obtained from the Eq. (57) by putting optimum inertia relation inside it and canceling out the oscillating term.

Eq. (71) gives an approximate analytical result for CMG with preferred inertia relation at Eq. (63). By just looking this simple equation, the effect of system parameters may

be interpreted. Firstly, if φ_0 and θ_0 are equal to each other there is a quadratic relation between angular velocity output and excitation amplitude (Figure 3.4). Secondly, there is a proportional relation with excitation frequency (Figure 3.3). The phase difference contributes to angular velocity gain with $sin\,\beta$ term. The plot of numerical sweep and approximate analytical solution graph of phase shift may be seen in Figure 4.4. There is a slight difference between the results of Eq. (50) and Eq. (71). This simple angular velocity equation may be used for control purposes.

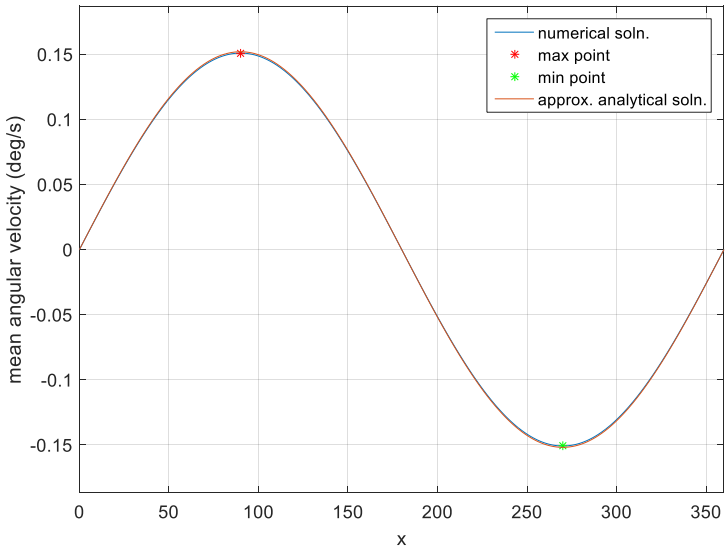

Figure 4.4. Comparison of exact and approximate analytical results of phase difference effect on angular velocity output

4.2.3. Possible Rotor Geometries

This relation between the principal mass moments of inertias of the rotor, given in Eq. (63) should eliminate the oscillations in the spacecraft output axis. A prism-shaped rotor geometry is selected to find possible rotor geometries which satisfy the preferred inertia relation in Eq. (63). The dimensions of this rotor are shown symbolically in Figure 4.5.

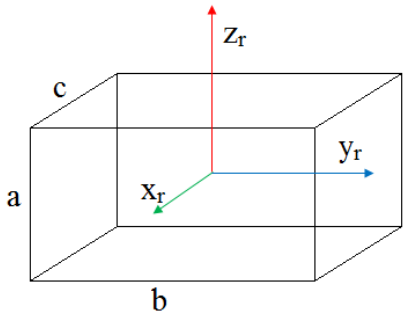

Figure 4.5. Rectangular prism rotor geometry with rotor reference frame

Then, the moment of inertias become,

$$J_r^{xx} = \frac{1}{12}m(a^2 + b^2) \quad J_r^{yy} = \frac{1}{12}m(a^2 + c^2) \quad J_r^{zz} = \frac{1}{12}m(b^2 + c^2) \tag{72}$$

Inserting into the inertia relation of Eq. (63) gives,

$$\frac{1}{12}m(a^2 + c^2) + \frac{1}{12}m(b^2 + c^2) \cong \frac{1}{12}m(a^2 + b^2) \quad \rightarrow \quad c \cong 0 \tag{73}$$

This means that rotor geometry must be a plate-like thin object where its surface normal is in the direction of the $\mathbf{x}_r$ vector (gimbal axis). The useful shape could be a thin disc where, $\mathbf{x}_r$, is the axis of rotation of the disc. On the other hand, a rod-like rotor geometry where the rod axis is oriented along the z-axis also closely satisfies the preferred inertia relation obtained.

4.2.4. Tip Point Trajectory of Slender Rod

The kinematics of the motion of the rod-like rotor geometry may further be investigated by looking at the trajectory of the tip point of the rotor. When 90° phase shift is given between rotor and gimbal axes, the following derivation may be done.

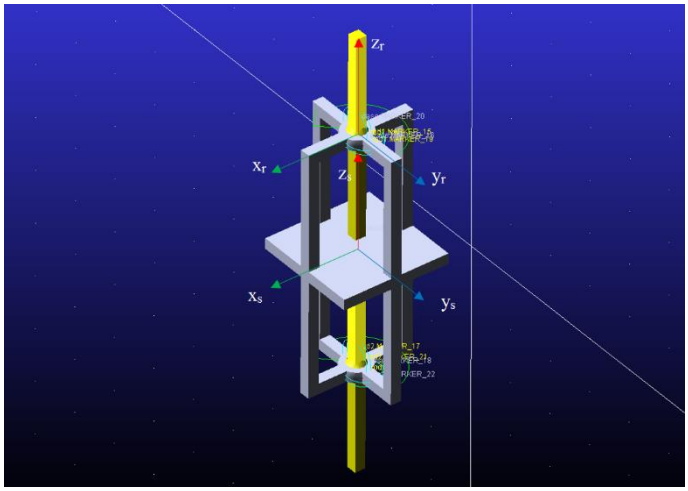

Figure 4.6. Simulation Model Constructed in ADAMS

Tip vector,

$$\vec{r} = a\vec{k} \tag{74}$$

Oscillatory inputs,

$$\varphi = \varphi_0 \sin 2\pi f t \tag{75}$$

$$\theta = \theta_0 \sin(2\pi f t + \beta) \tag{76}$$

The position of the tip of the rod-like rotor in the spacecraft fixed frame is,

$$\vec{r}_{rot} = T_\theta T_\varphi \vec{r} \tag{77}$$

$$\vec{r}_{rot} = \begin{bmatrix} a\cos\varphi\sin\theta \\ -a\sin\varphi \\ a\cos\varphi\cos\theta \end{bmatrix} \tag{78}$$

With oscillatory motions,

$$\vec{r}_{rot} = \begin{bmatrix} \mathrm{a}\cos(\varphi_0 \sin 2\pi f t)\sin(\theta_0 \sin(2\pi f t + \beta)) \\ -\mathrm{a}\sin(\varphi_0 \sin 2\pi f t) \\ \mathrm{a}\cos(\varphi_0 \sin 2\pi f t)\cos(\theta_0 \sin(2\pi f t + \beta)) \end{bmatrix} \tag{79}$$

Assuming small angle oscillations, cosine terms drop,

$$\vec{r}_{rot} \cong \begin{bmatrix} \mathrm{a}\theta_0 \sin(2\pi f t + \beta) \\ -\mathrm{a}\varphi_0 \sin 2\pi f t \\ \mathrm{a} \end{bmatrix} \tag{80}$$

Assuming $\varphi_0 = \theta_0$ and $\beta = 90°$

$$\vec{r}_{rot} = \begin{bmatrix} \mathrm{a}\varphi_0 \cos 2\pi f t \\ -\mathrm{a}\varphi_0 \sin 2\pi f t \\ \mathrm{a} \end{bmatrix} \tag{81}$$

The trajectory of the above vector tip gives a circle. For different phase shifts, tip trajectories obtained are plotted in Figure 4.7. The half-length of the rotor is taken as 100 units and vibration amplitudes of the rotor and gimbal axis are 5°. The orange line for 90° phase shift deviates only $2.4\ 10^{-4}$ % from an exact circle. It may be also seen that for 0° phase shift the tip point of rotor only oscillates on the blue line in the middle and no angular momentum generated on the rotor and spacecraft. Geometrically speaking, up to 90° phase difference, the total angular momentum built on the rotor gradually increases and reaches a maximum at the 90° phase difference. Numerically, it was shown that 90° phase difference gives maximum angular velocity gain. By looking at this figure, it may be concluded that the amount of precession of the rotor mass increases with increasing phase difference up to 90°.

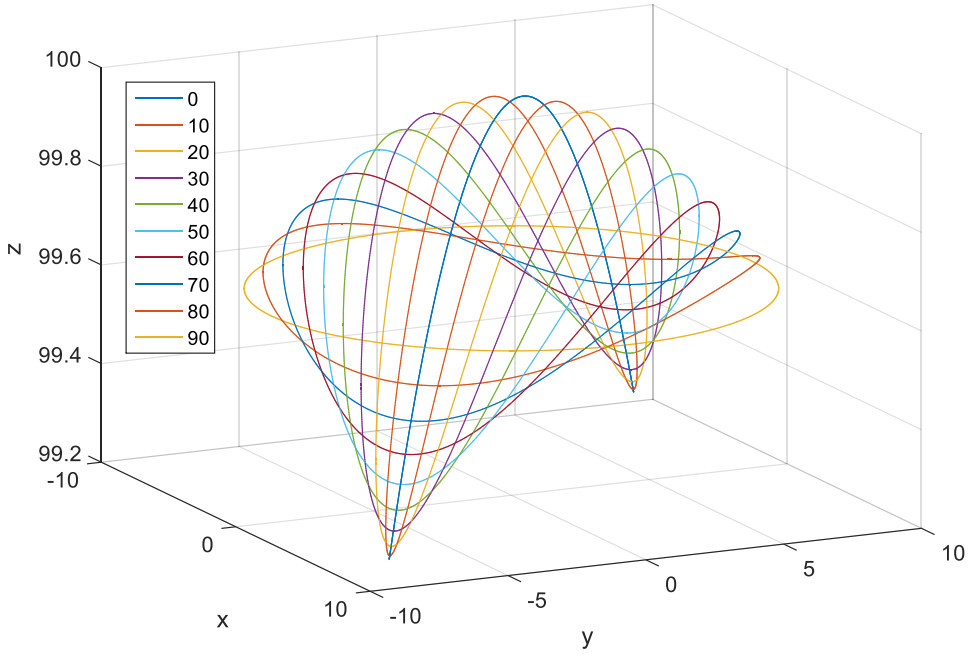

Figure 4.7. The trajectory of the tip point of the rotor from 0° to 90° phase differences

4.2.5. Comparison of Rotor Performances

The system is modeled and simulated in the ADAMS software environment. A pair of CMG actuators, excited in an out of phase manner with respect to each other, are used to cancel out excitations along x_s and y_s axis. The ADAMS simulation drawing is given in Figure 4.6. The gimbal body was not drawn. However, gimbal axis connections are realized using universal joints between the spacecraft body and rod-like rotor body.

For simplicity, fully symmetric spacecraft body is employed. Due to universal joint used, the rod does not rotate around z_r. However, it can rotate around x_r which is gimbal axis and y_r which is rotor axis. In the ADAMS model, the aluminum material is selected for the rods and spacecraft body is cast iron (gray). The inertia matrix of the rods then becomes,

$$J_r = \begin{bmatrix} 1.573269E-004 & 0 & 0 \\ 0 & 1.573269E-004 & 0 \\ 0 & 0 & 1.246951E-006 \end{bmatrix} kg \cdot m^2$$

Thus, the calculated inertias closely satisfy the relation $J_r^{yy} + J_r^{zz} \cong J_r^{xx}$. 10 Hz, 0.1 rad (~5.73°) amplitude sinusoidal motions applied to the rotor and gimbal axis. Upper and lower CMGs operate in out of phase manner and individual CMGs has a 90° phase shift between their own rotor and gimbal axes. Amplitudes of vibrations are gradually increased between 0-2 secs and decreased between 5-7 secs. The simulation results are presented in Figure 4.8, shows that the spacecraft z-axis attains an angular velocity as the oscillation amplitudes are increased, and the reaction oscillations in the other two axis are successfully cancelled and do not exist.

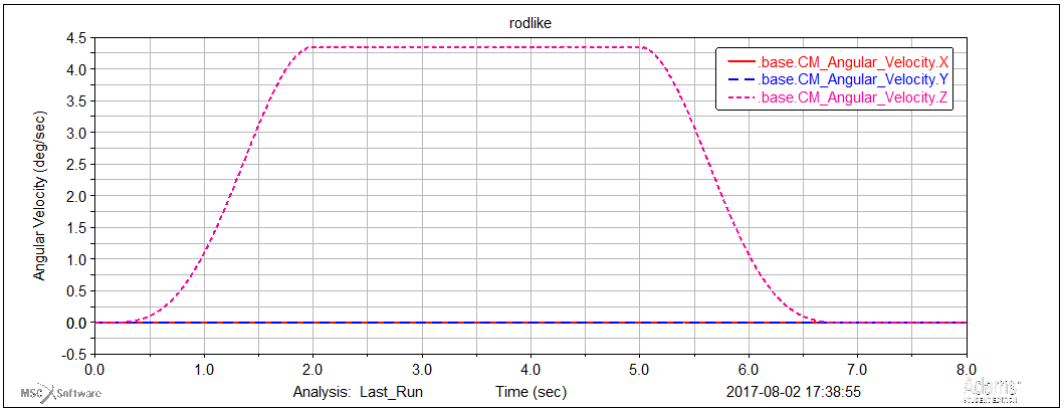

Figure 4.8. Simulation results with two out of phase CMGs with slender rod rotor geometry

To demonstrate the effects of inertia on the response, a spherical or cube-shaped rotor with inertia properties given below is also used by changing z component of previous slender rod's inertia matrix,

$$J_r = \begin{bmatrix} 1.573269E-004 & 0 & 0 \\ 0 & 1.573269E-004 & 0 \\ 0 & 0 & 1.573269E-004 \end{bmatrix} kg \cdot m^2$$

The output with the spherical rotor is presented in Figure 4.9 together with the rod-like rotor. The green line in the figure gives the satellite z-axis angular velocity when a cube-shaped or spherical rotor is used. As it may be observed from the figure, the useful angular velocity output oscillates between 0°/s and 4°/s and its mean value is about 2°/s. On the other hand, the magenta line shows the previous rod-like rotor output. There are three advantages obtained when a rod-like rotor design is used.

- The total mass of the rotor is reduced.
- The mean angular velocity increased attained by the satellite is two times higher.
- The oscillations on the angular velocity output almost dropped to the zero.

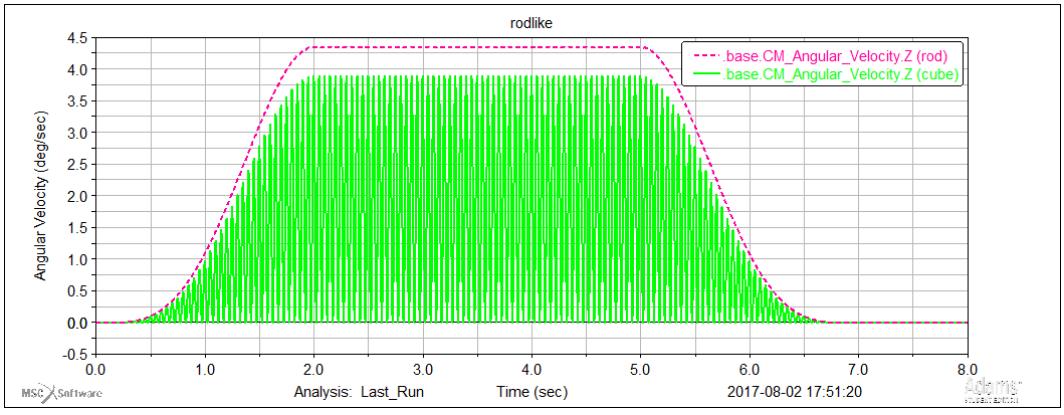

Figure 4.9. Satellite response with the spherical rotor and long slender rotor CMGs

In the Figure 4.10 and Figure 4.11, angular accelerations on both rotor configurations are given. For cube shaped rotor geometry, angular acceleration amplitude is around 250°/s^2 but for the rod, it is only about 1.1°/s^2. This further demonstrates that, at steady

state, the oscillatory torque generated by the CMG drastically drops and spacecraft moves smoothly on the desired rotation axis when a rod type rotor is used.

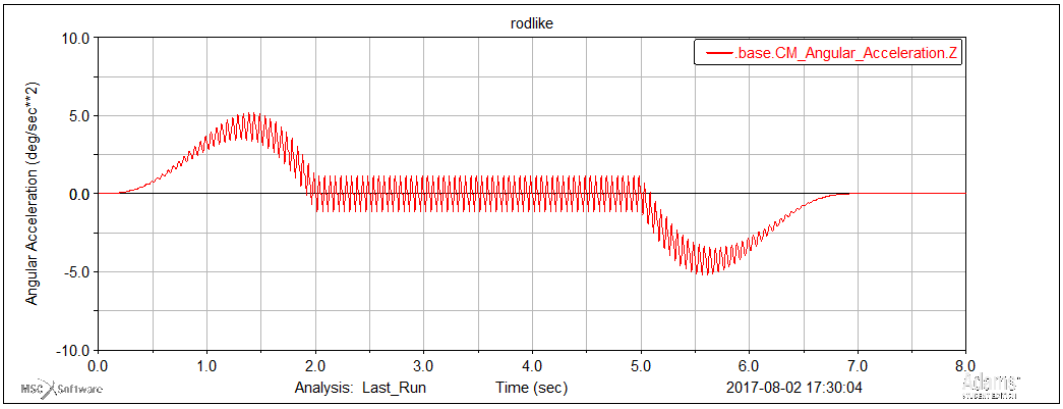

Figure 4.10. Angular acceleration on the spacecraft axis by using slender rotor geometry

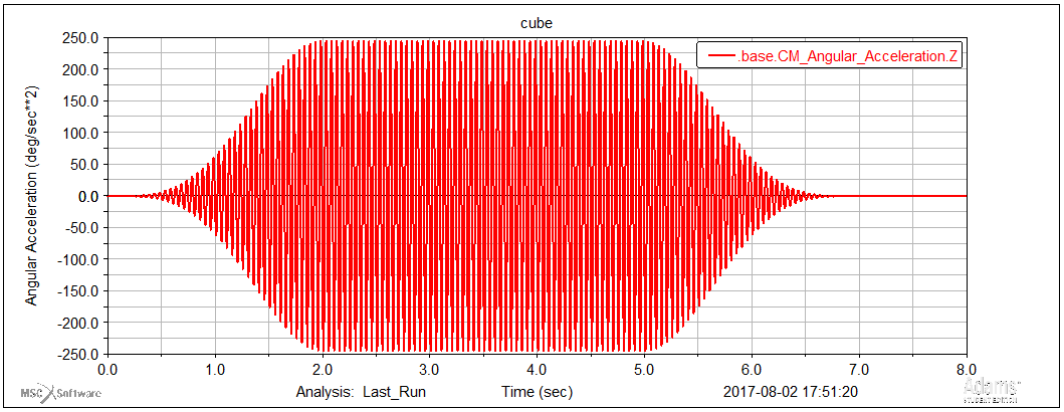

Figure 4.11. Angular acceleration on the spacecraft axis by using cube rotor geometry

A set of simulations are carried out to demonstrate the effect of making slender CMG on the output axis performance. For this purpose, first, a cube-shaped rotor is used. The rotor base area is gradually reduced while the x-axis is increased such that the rotor mass is kept constant (Figure 4.12). The simulation results are presented in Figure 4.13. It may be seen from this figure that, as the rotor becomes slender, the satellite slew velocity increases. In addition, the oscillations along this axis are also reduced. These results are also tabulated in *Table 4.1*. The change in oscillations and the mean value of the angular velocity along the satellite z-axis may be observed from the table. Numerically, the mean value of the angular velocity obtained with different

rotors changes from 0.082°/s for the cube rotor to 8.19°/s for a slender rotor which is 10 times taller and angular velocity almost increased 100 times. The oscillations also decreased from 100% for a cube rotor, to less 0.15% for the slender rotor.

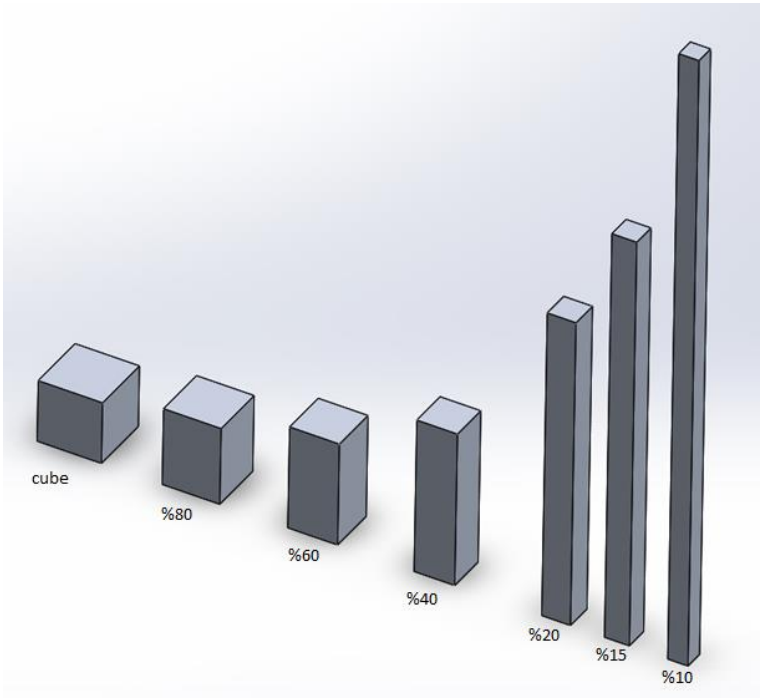

Figure 4.12. Changing rotor shape with the same mass

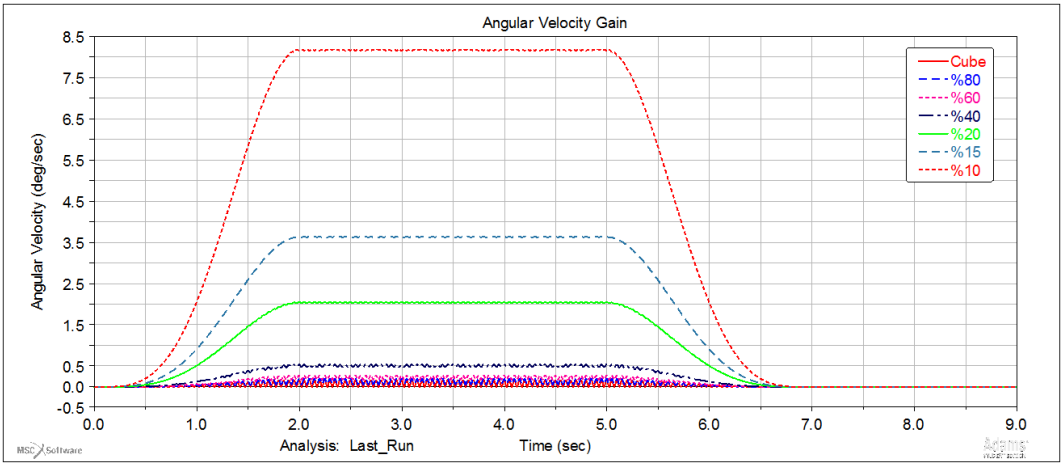

Figure 4.13. The angular velocity of satellite obtained with different rotor geometries

Table 4.1. *The effect of rotor geometry on the output angular velocity and fluctuation*

	Dimensions (mm)	Ix (kg.m^2) X 10^{-12}	Iy (kg.m^2) X 10^{-12}	Iz (kg.m^2) X 10^{-12}	Wmax (deg/s)	Wmin (deg/s)	W average (deg/s)	W fluctuation	
								(deg/s)	%
Cube	26.5 x 26.5 x 26.5	5.8	5.8	5.8	0.1629	0	0.0821	0.1629	100
%80 base area	23.7x23.7x33.1	6.8	6.9	4.7	0.1926	0.0626	0.1281	0.1300	50.74
%60 base area	20.5x20.5x44.1	9.8	9.9	3.5	0.2755	0.1786	0.2274	0.0969	21.31
%40 base area	16.7x16.7x66.1	19.4	19.4	2.3	0.5427	0.4799	0.5122	0.0628	6.13
%20 base area	11.8x11.8x132.3	73.5	73.5	1.17	2.0573	2.0349	2.0470	0.0224	0.55
%15 base area	10.2x10.2x176.4	130.1	130.0	0.88	3.6405	3.6333	3.6381	0.0072	0.1
%10 base area	8.4x8.4x264.6	292.0	292.0	0.58	8.1887	8.1639	8.1797	0.0248	0.15

CHAPTER 5

EXPERIMENTATION

Two experiments were performed to observe the dynamics of the actuator. First one has totally arbitrary rotor geometry to investigate the most general case and the second one consists of two actuators with slender rod rotor geometry.

5.1. Test Setup with Arbitrary Inertia Values

For the first iteration, a test prototype with arbitrary inertia values was modeled in SolidWorks and manufacturing has been done using CNC milling machines.

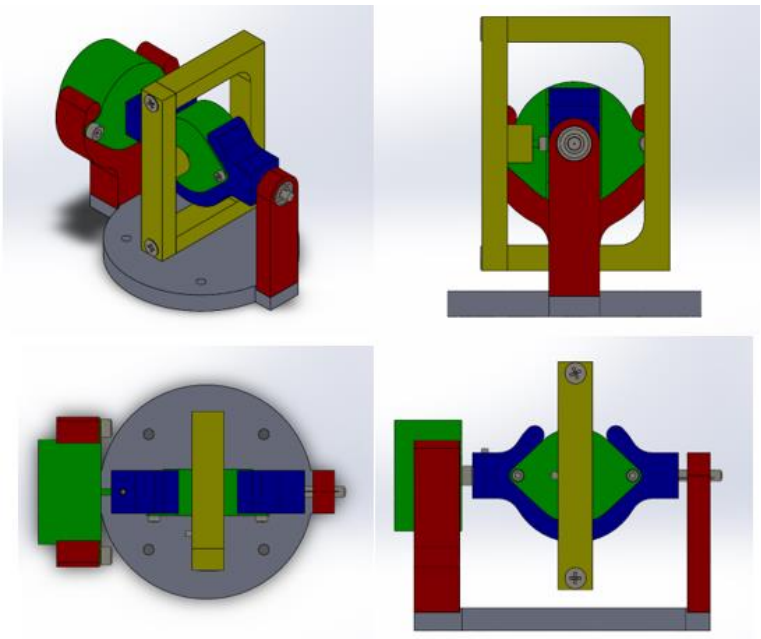

Figure 5.1. CAD model of the test prototype

The produced prototype of the actuator is presented in Figure 5.2. The rotor and gimbal axes are actuated by stepper motors (green). The step angles of the chosen stepper motors are 7.5°. Sinusoidal voltage inputs are generated with the desired phase shift and applied to the single coil group of the stepper motors. When a sinusoidal signal is applied to a single coil group of the stepper motor, it is expected that it starts

vibrating within two steps. Since, with the applied excitation, the coil becomes an electromagnet which changes its poles with a specified frequency, it rotationally vibrates the rotor of the stepper motor.

After several tests with sinusoidal inputs, it was realized that it is impractical to control the vibration of stepper motors within a single step. This is due to the fact that steps can be missed and the continuous rotation of stepper motors may occur. Hence, the design is augmented by attaching restoring springs to the gimbal and rotor axes (Figure 5.3). In this way, the stepper motors can only vibrate within a single step amplitude.

The actuator was attached to the air bearing to reduce the friction on the CMG output axis. The air bearing is mounted on a heavy platform to minimize vibrations on the gimbal and rotor axes due to excitation. Moreover, this platform was balanced to have a horizontal orientation with respect to the ground hence the effect of gravity is mitigated. Sinusoidal inputs are generated by a high-resolution NI PCI-4461 signal generator card. A voltage follower operational amplifier circuit was constructed to buffer the output signals of the signal generator card. DC power supply was used to feed power to the op-amps. Amplified signals are transmitted via very thin cables suspended above the actuator to reduce the spring effect of these cables. The useful rotation on the air bearing rotation axis was measured by Polytech scanning vibrometer with PSV-400 scanning head. The vibrometer laser beam was aligned perpendicular to a vertical surface of the rotor to measure the linear velocity of this point. For small angles, this linear velocity may easily be converted to angular velocity by dividing the perpendicular distance between the laser spot and the rotation axis of the air bearing. Complete setup can be seen in Figure 5.4.

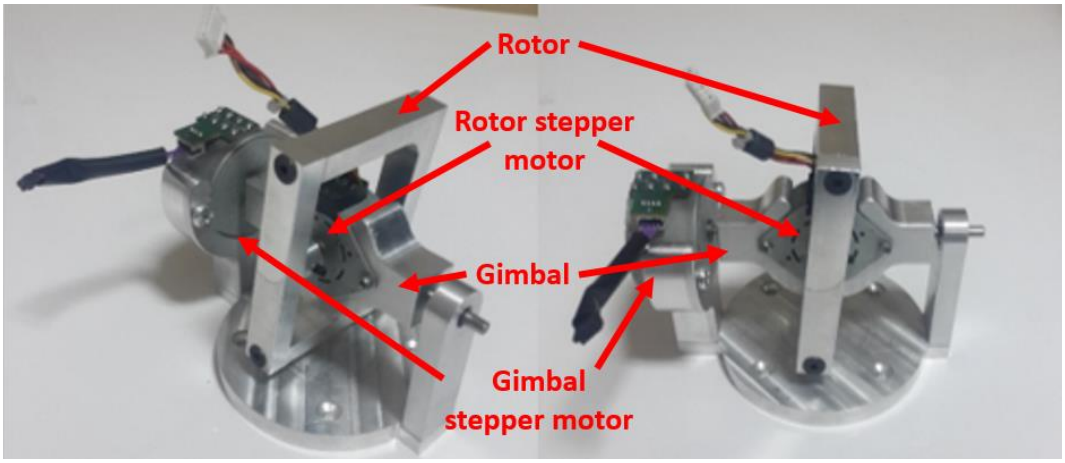

Figure 5.2. Manufactured CMG prototype

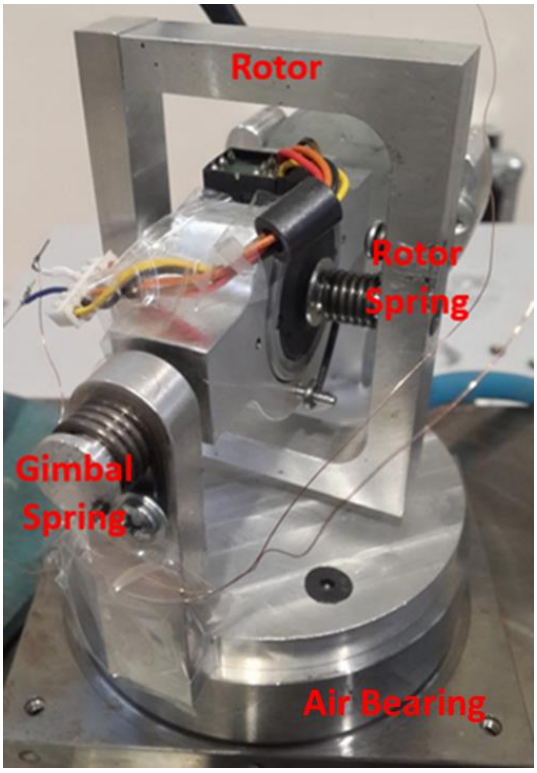

Figure 5.3. Restoring springs for gimbal and rotor axes

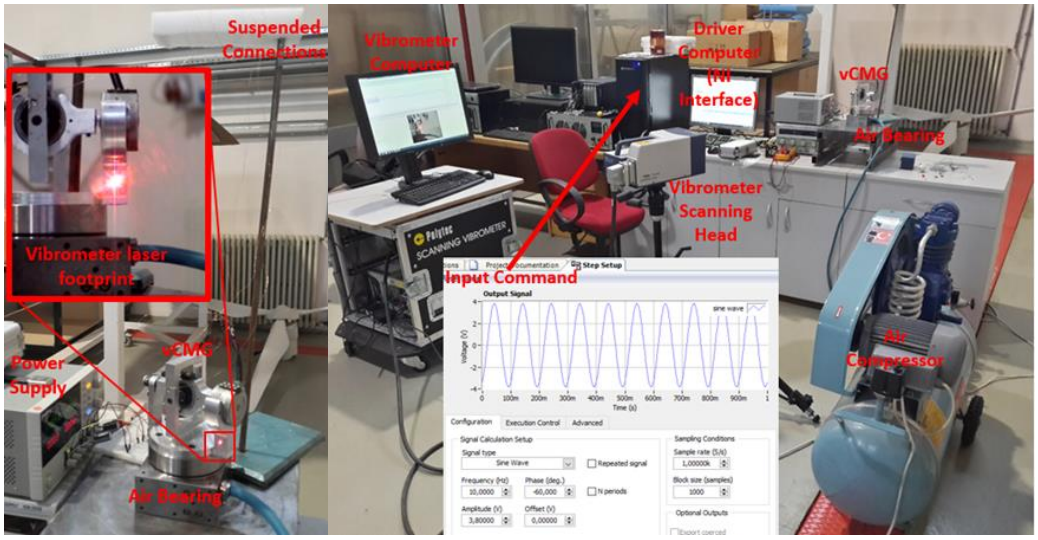

Figure 5.4. Actuator, air bearing and position of laser footprint (left). The general architecture of the setup is presented on the right

The experiments were conducted for various phase differences and obtained angular velocities are presented in Figure 5.5. The graphs present the results of four separate experiments. The difference between these experiments is the phase shifts between the sinusoidal excitation applied to the gimbal and rotor axes. The air bearing, together with the CMG only vibrates around its original position for in-phase excitation. As the phase difference between the sinusoids applied to the gimbal and rotor axis is increased, mean velocity increases.

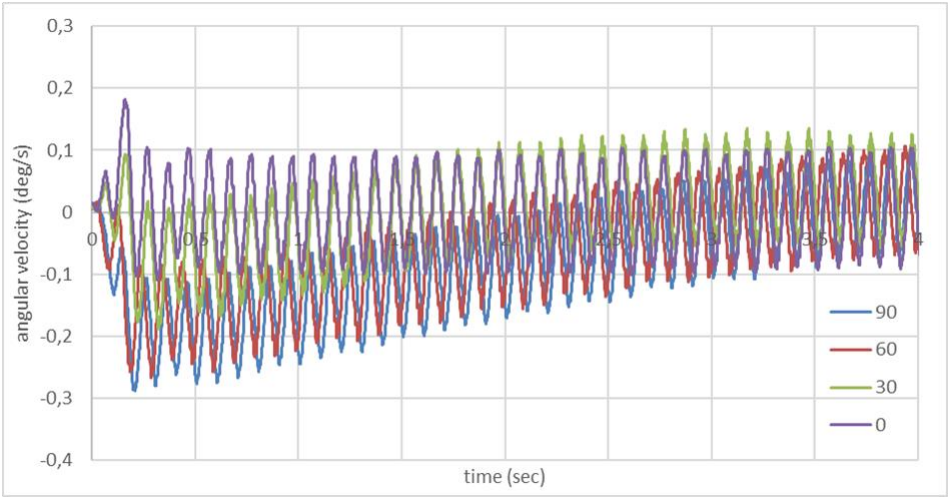

Figure 5.5. Angular velocity results for 0°, 30°, 60° and 90° phase differences

From the results presented in Figure 5.5, it may be observed that the angular velocities gradually drop to zero in time. The possible reasons for this behavior are, small but nonzero spring effect caused by the suspended signal cables of motors, the unbalance on the platform, and damping inside the air bearing due to air flow. Together with the spring effect by suspended cables and gravitational effect due to slight unbalance on the platform, the angular position of air bearing returns to its equilibrium position afterward. However, when the bearing returns to its equilibrium position, the amount of the angular momentum stored on the rotor of the CMG may be observed by instantly cutting the power supplied to the rotor and gimbal axes' motors. When the power is shut down, the gimbal and rotor springs, internal frictions on the excitation axes and damping, slows down the rotor and gimbal vibration immediately. Response forces and torques are induced on the air bearing axis back again. The following figure shows the amount of angular velocity gained by air bearing when the system is shut down at the reached equilibrium position. For 0° phase difference, the Z-axis (spacecraft) component of the angular momentum of the rotor is zero. Hence, there is no net torque response on the air bearing axis after cutting off power and net angular velocity of the air bearing is zero. The angular velocity response at equilibrium increases from 0° to 90°.

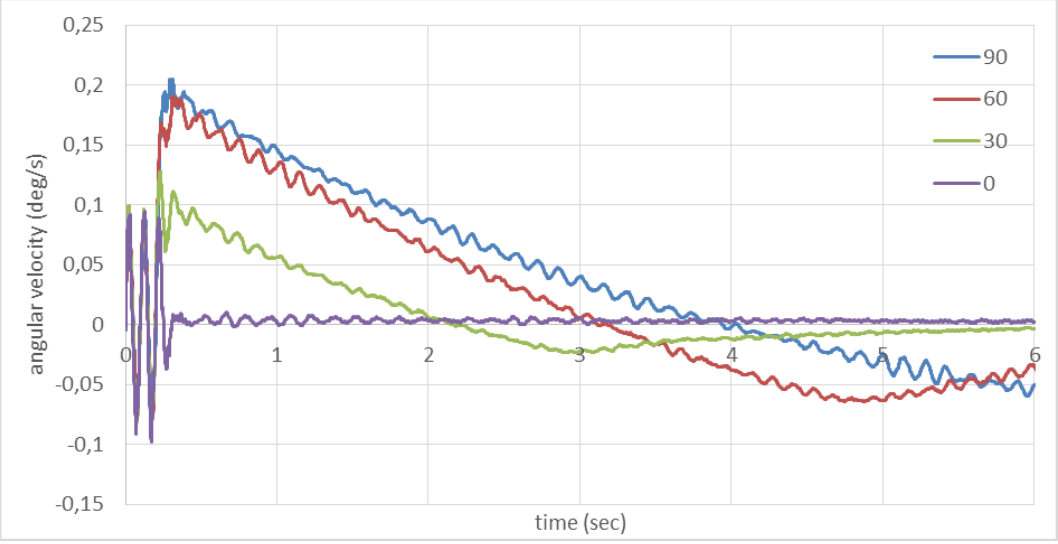

Figure 5.6. Angular velocity results for 0°, 30°, 60° and 90° phase differences after shutdown

Additional results are presented from Figure 5.7 to Figure 5.10, for phase differences from 0° to 360° are given in 10 degree increments. From these results, it may be observed that no net angular momentum is shed for 180° phase difference just like the 0° phase difference case. For phase difference from 180° to 360°, the angular momentum transferred to the air bearing is reversed. Thus, it may be concluded that, by negating the phase difference, the air bearing (or satellite) rotation direction may be changed. These results are also in line with the observations obtained from the simulations. The expected angular velocities obtained from the mathematical model and experiments were presented in Figure 5.11. From the figure, it may be observed that the mathematical model and the experiment yields the similar trends although the angular velocity magnitudes are different.

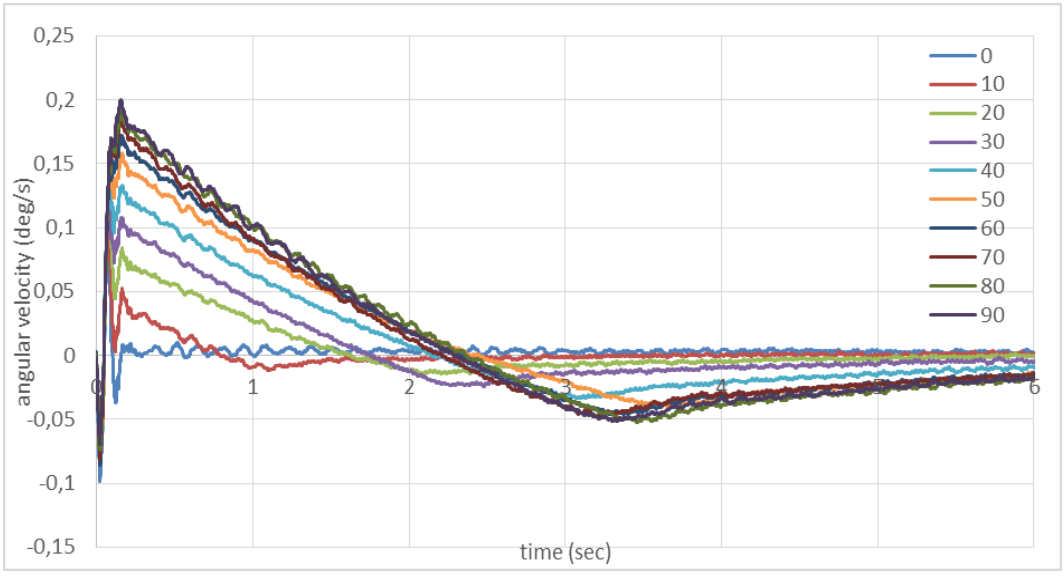

Figure 5.7. Angular velocity gains for 0° to 90° phase differences after shutdown

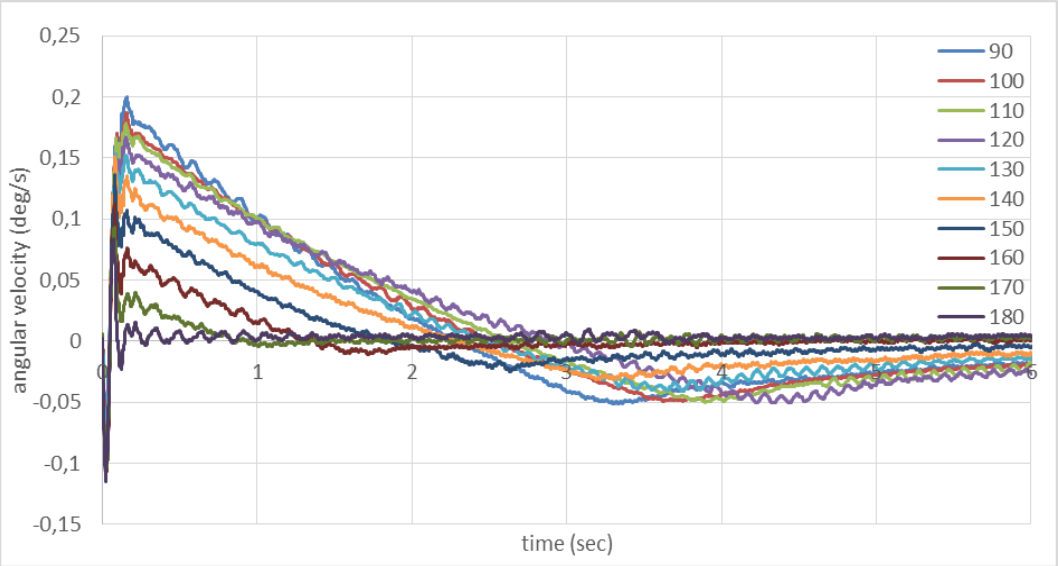

Figure 5.8. Angular velocity gains for 90° to 180° phase differences after shutdown

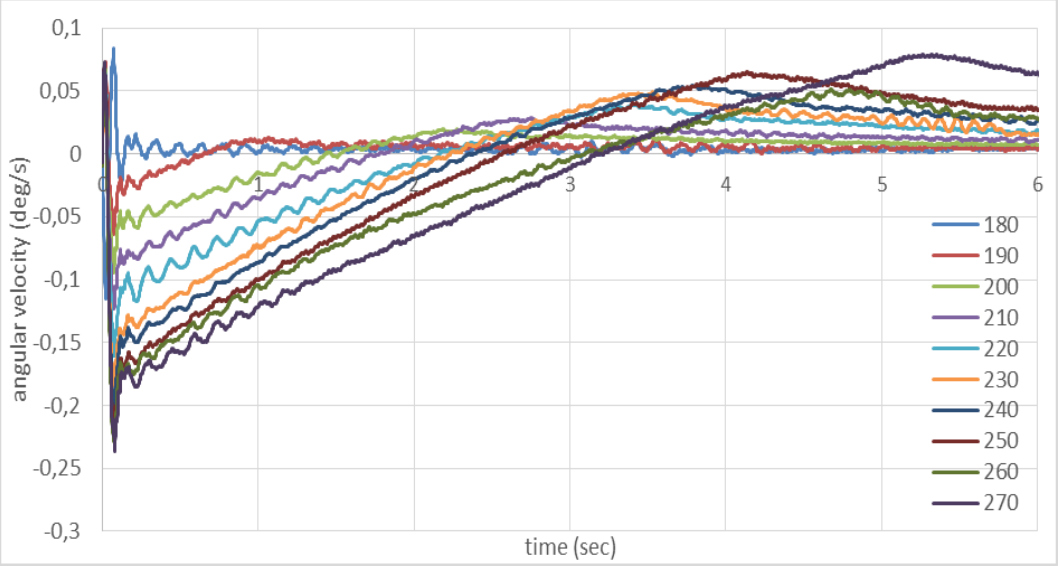

Figure 5.9. Angular velocity gains for 180° to 270° phase differences after shutdown

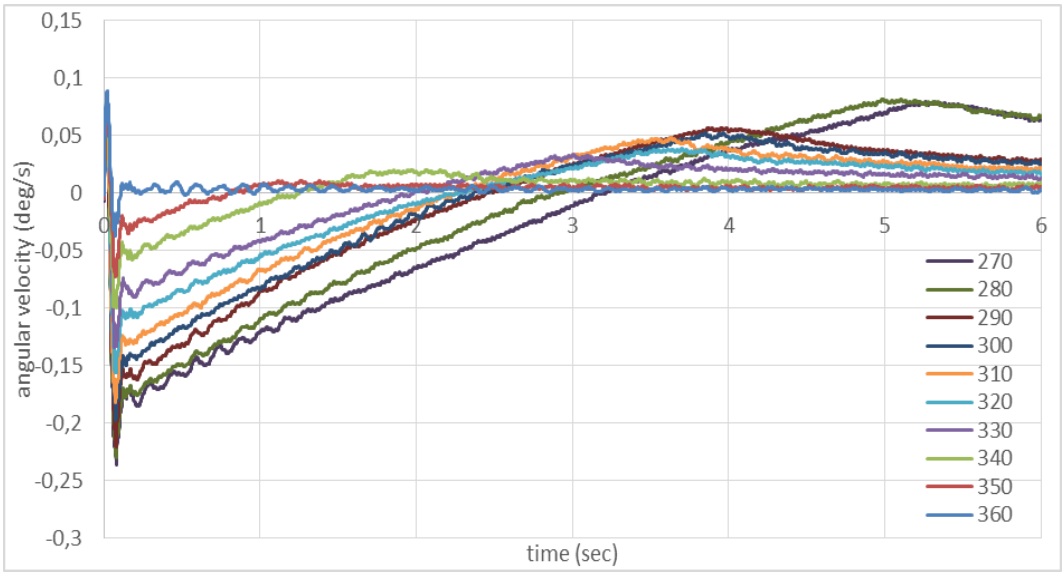

Figure 5.10. Angular velocity gains for 270° to 360° phase differences after shutdown

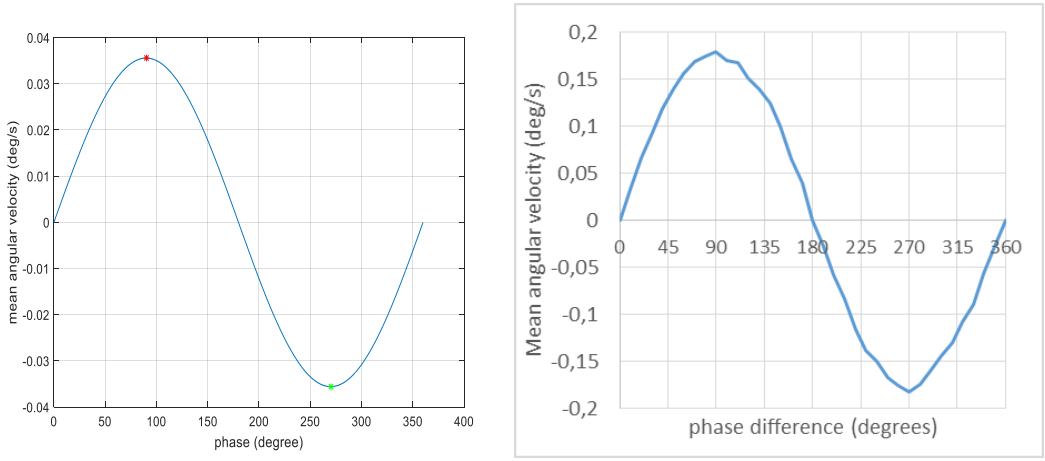

Figure 5.11. Effect of phase difference on mean angular velocity from 0° to 360° (Mathematical result on the left, experimental result on the right)

The experimental results were compared with ADAMS simulation. First, the required inertia parameters of the experimental setup are obtained from the CAD models.

$$I_{gimbal} = \begin{bmatrix} 36827.75e-9 & 0 & 0 \\ 0 & 108327.90e-9 & 0 \\ 0 & 0 & 88046.18e-9 \end{bmatrix} kg.m^2$$

$$I_{rotor} = \begin{bmatrix} 250427.92e-9 & 0 & 0 \\ 0 & 157607.89e-9 & 0 \\ 0 & 0 & 97674.44e-9 \end{bmatrix} kg.m^2$$

In the above matrices, the inertia of the gimbal and rotor motors are not included.

The rotor inertia of the rotor motor should also be estimated because it contributes to the inertia of the CMG rotor. An approximate inertia estimation for moving part (magnets) of rotor motor estimated from geometry as:

$$I_{magnets} = \begin{bmatrix} 2470.59e-9 & 0 & 0 \\ 0 & 1972.38e-9 & 0 \\ 0 & 0 & 2470.59e-9 \end{bmatrix} kg.m^2$$

The inertia of the spacecraft axis was obtained by using parallel axis theorem. Since the center of the mass of the CMG is not on the rotation axis of the air bearing. The moment of inertia of the air bearing rotor is 0.0052 kg.m^2. Then, the total moment of inertia along the rotation axis is estimated as,

$$I_{sc} = 6.982687 \times 10^{-3} kg.m^2$$

The other two inertia terms are not considered since it is a single axis air bearing. Voltages given to the motors were properly adjusted such that the vibration amplitudes of the axes are about 5°. In the simulations 6° amplitudes given to rotor and gimbal axis. Gimbal and rotor motors can supply 125 N.mm and 80 N.mm maximum torques, respectively. The spring constants of the restoring springs of gimbal and rotor axes are approximately calculated as 1.05 N.m/rad and 0.57 N.m/rad, respectively.

Finally, due to the spring effect of suspended power cables, unbalance of the air bearing platform and viscous friction inside air bearing, external torques occurred on the air bearing rotation axis. Hence, a spring and damper coefficient values are needed

on the air bearing (spacecraft) rotation axis to consider these torques. Assuming a linear behavior, the air bearing rotor equation may be written as,

$$I_{z(total)}\ddot{\gamma} + c\dot{\gamma} + k\gamma = 0 \quad with \ \gamma(0) = 0 \ and \ \dot{\gamma}(0) = \omega_{initial} \tag{82}$$

As mentioned in the previous results, after shutting down the power of the motors when the system is at equilibrium, the system tries to return its original equilibrium in a vibratory fashion. The 90° phase difference velocity measurement data is integrated to obtain the angular position graph.

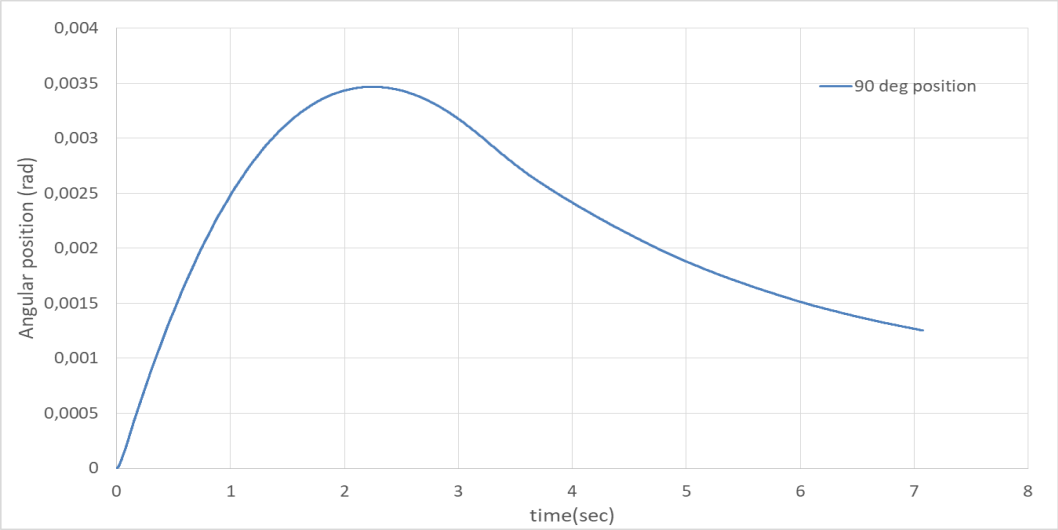

Figure 5.12. The position of spacecraft from equilibrium position after power shutdown while 90° phase difference applied

After some tuning of c and k values, it is observed that the air bearing rotation axis is close to the critically damped system. By using excel solver and least squares regression, a critically damped solution curve is fitted with the experimental result.

$$\gamma(t) = e^{-\omega_n t}\omega_0 t \qquad where$$
$$\omega_0 = 0.003497\frac{rad}{s} \quad by\ experiment\ result \tag{83}$$

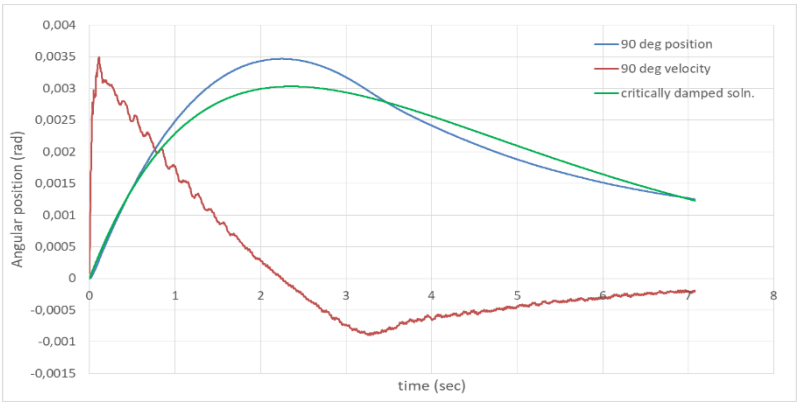

Figure 5.13. Critically damped solution curve fitted to the experimental result

Due to the nonlinear behavior of the system, it is impossible to fit a linear solution perfectly to the experimental result. However, this solution satisfies and realizes the experimental result with an acceptable error. After this curve fitting procedure, the stiffness and damping on the air bearing rotation axis becomes;

$$c_{air} = 0{,}006017 \frac{Nms}{rad}$$

$$k_{air} = 0.001277 \frac{Nm}{rad}$$

Together with all these systems parameters, simulations were done by using ADAMS.

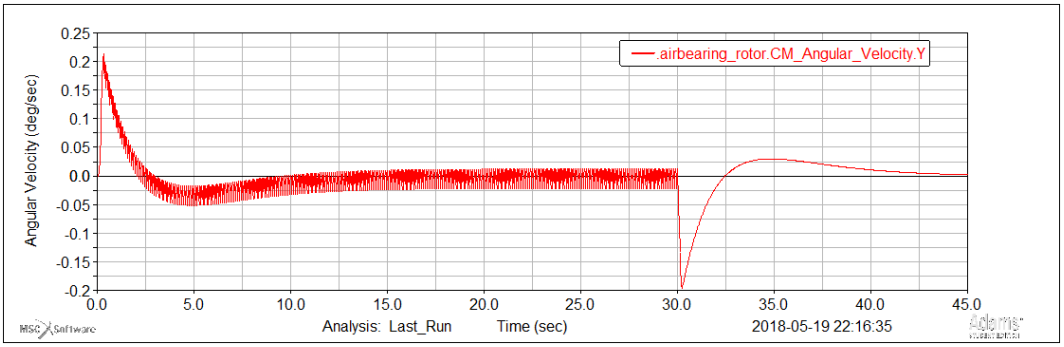

Figure 5.14. ADAMS simulation results with experiment setup mechanical properties

ADAMS simulation results show close numerical values and trends with respect to experimental results for 90° phase difference. Around 0.2°/s maximum angular velocity gain was obtained just like in the experimental results.

5.2. Test Setup with Slender Rotor Geometry

In the equation Eq. (63), it has been shown that vibratory CMG shows better performance with preferred inertia values for rotors. According to this result, a new mechanical design has been performed. It consists of two actuators with slender rod rotor geometry. A balancing table was also designed to reduce gravitational effects on the axis of the air bearing.

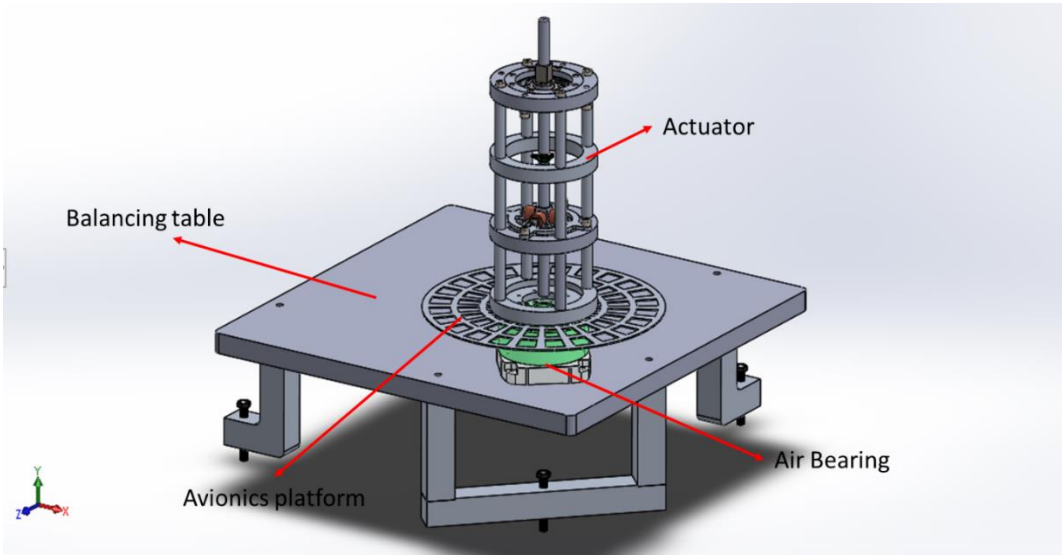

Figure 5.15. Mechanical design of experiment setup for slender rotor geometry

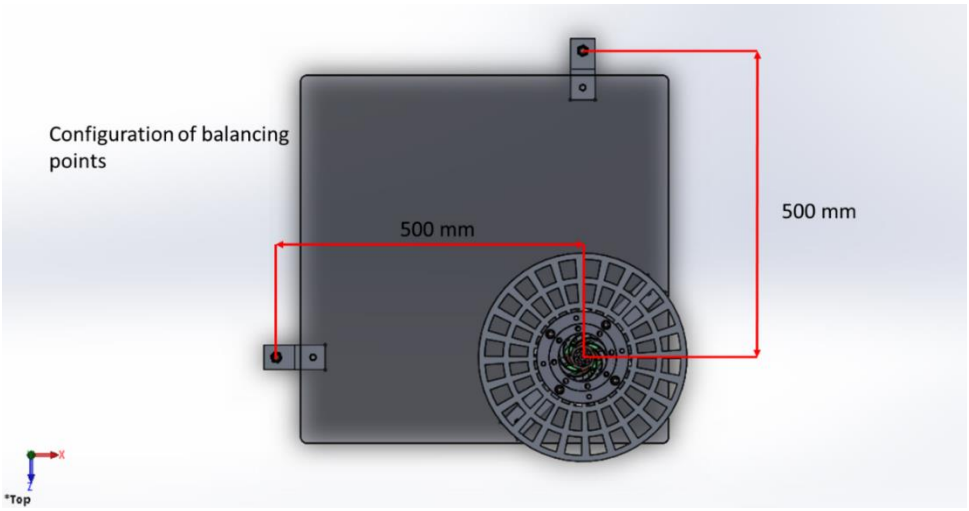

Figure 5.16. The configuration of balancing points

The balancing table has three legs and touches to ground with sharp-edged M10 bolts to adjust the level of table perpendicular to the gravity field. One leg is just top of the axis of rotation and the other two were separated 500 mm apart. The positions of the other two legs are just on the corners of a 500x500 mm square. Thanks to this configuration, the table can be balanced just with two axes and these axes are decoupled. The calibration of one axis is not affected while the orientation of other axis is changed. This eases the leveling operation of the table. The slope of balancing table changes 0.172° for one revolution of bolts.

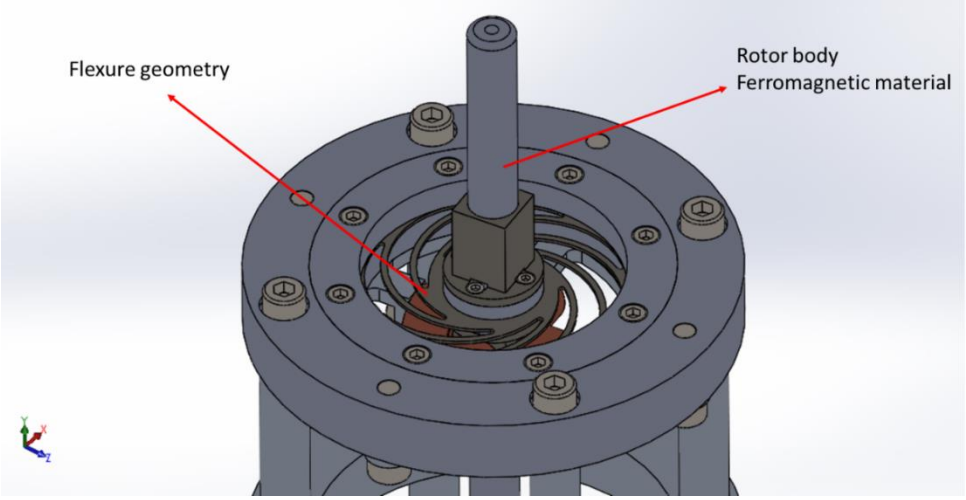

Figure 5.17. Flexure design and rotor geometry

In the design of actuator, gimbal geometry was completely removed and only rotor body has been designed. Because it has been seen that the gimbal body does not have any effect on output angular velocity of the spacecraft body when Eq. (50) is investigated. On the other hand, the degree of freedom of gimbal is given kinematically using flexure geometry (Figure 5.17). Flexure geometry has been designed for 20-25 Hz resonance frequency range. The material of flexure is 1 mm thick AISI 1075 sheet. Rotor body was made of AISI 1040 steel.

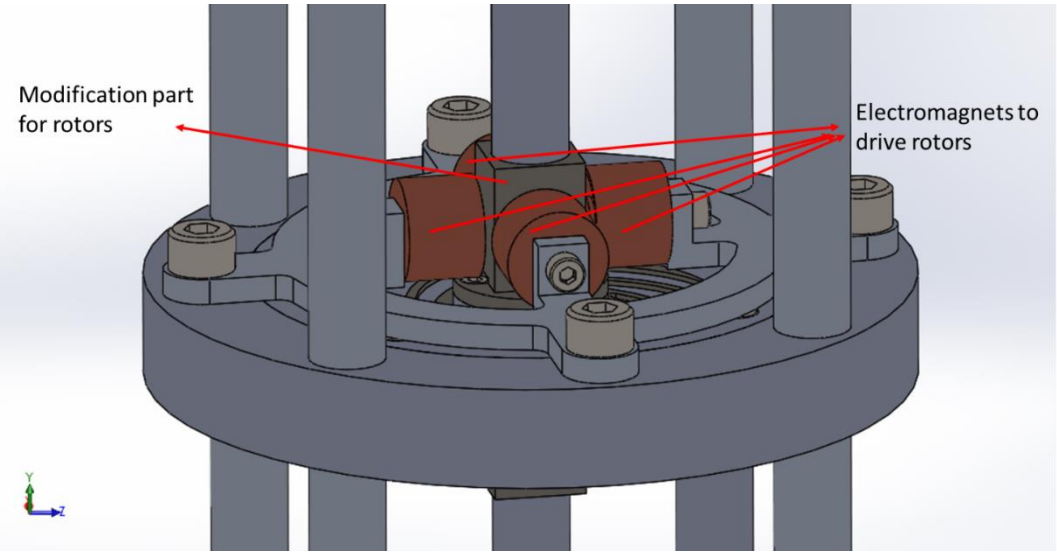

Figure 5.18. Located electromagnets to drive rotors and modification piece added to rotor geometry to increase the performance of electromagnets

Electromagnets were used to drive rotors without any contact. Chosen electromagnets are capable of holding 24.5 N load. In Figure 4.7, it has been shown that the tip of slender rod rotor geometry draws a trajectory that is close to the circle when 90° phase difference is given between the rotor and gimbal axes. As a result, rods actually performs precession motion for 90° phase difference.

After manufacturing, the first test was done to check holding performance of magnets. However, it was not enough for the desired vibration amplitudes. Hence, a modification piece was manufactured to decrease the distance between the magnetic fields and the rotor surface. In addition to this, electromagnets work better on flat surfaces. Due to this reason, the modification piece was designed as a square prism with flat side surfaces to increase the performance of the magnets (Figure 5.18). The material was chosen AISI 1010 low carbon steel for better ferromagnetic properties.

Including the modification part, the first two resonance frequency of CMGs were found via COMSOL. Results may be seen in Figure 5.19. Two resonance frequencies are very close to each other and describe the degree of freedom of gimbal and rotor revolute joints, kinematically.

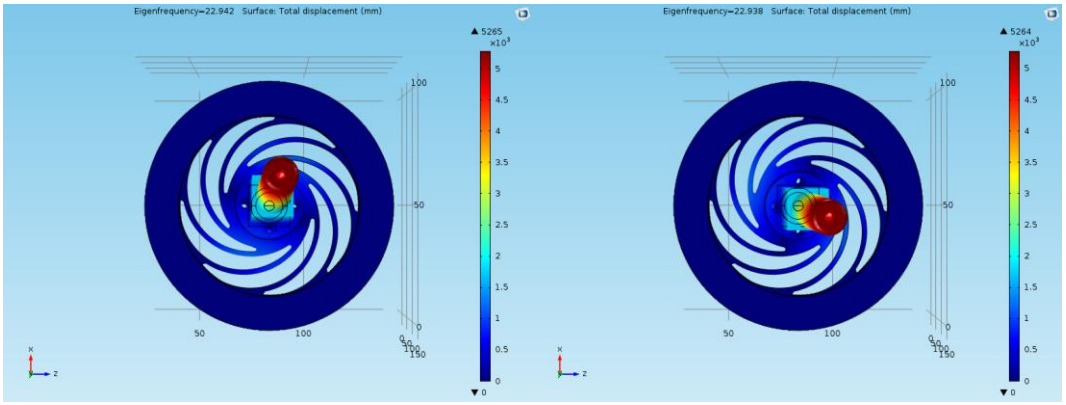

Figure 5.19. First two resonance frequencies of flexure geometry (22.942 Hz and 22.938 Hz)

Fatigue analysis of designed flexure geometry should also be performed for long-term operation.

The resonance frequencies of upper and lower CMGs were found by using Polytech Scanning Vibrometer mentioned in the previous experiment. Firstly, the electromagnets were demounted and impact response tests were done for upper and lower CMGs separately. Vibrometer measures linear velocity of the rotor and calculates FFT of the measured velocity of the rotors after impacts. Obtained frequency resolution for FFT is 0.25 Hz.

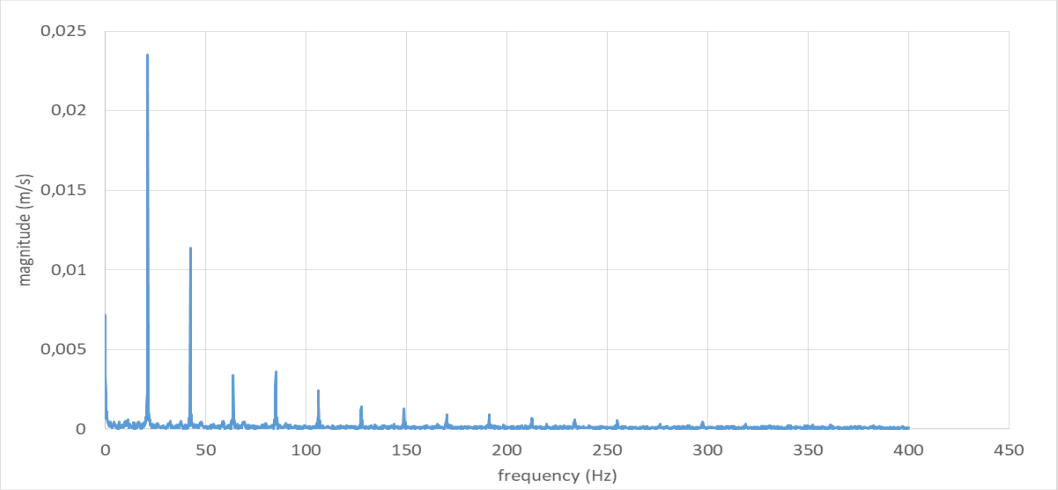

Figure 5.20. Impact test FFT result of upper CMG without electromagnets (21.25 Hz first fundamental frequency)

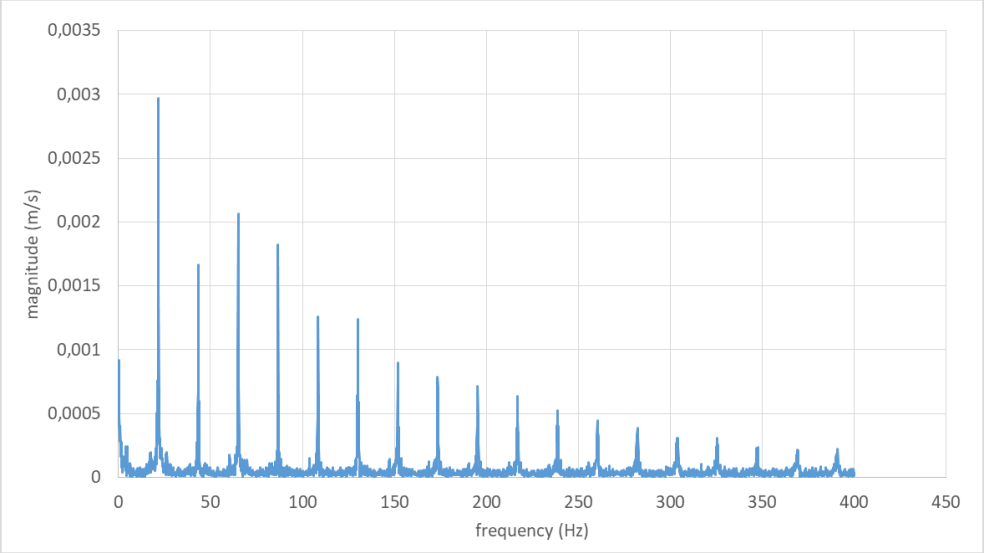

Figure 5.21. Impact test FFT result of lower CMG without electromagnets (21.75 Hz first fundamental frequency)

It can be seen from Figure 5.20 and Figure 5.21 that measured fundamental frequencies of designed flexure geometry is very close to each other. The results are also very close to the simulation results of COMSOL in Figure 5.19. However, there are higher frequencies with multiples of fundamental frequency as noise. The same impact tests were also done by mounting electromagnets. Electromagnets were not excited.

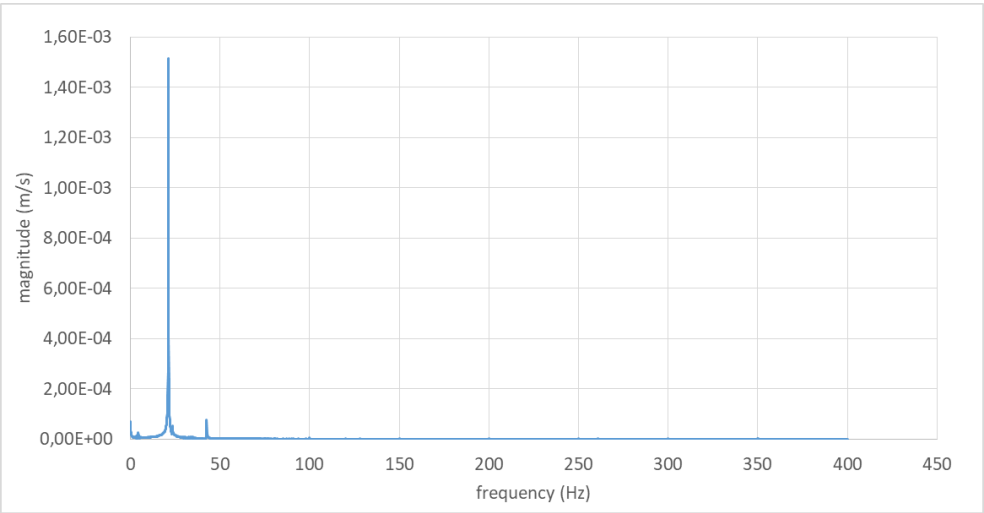

Figure 5.22. Impact test FFT result of upper CMG with electromagnets (21.25 Hz first fundamental frequency)

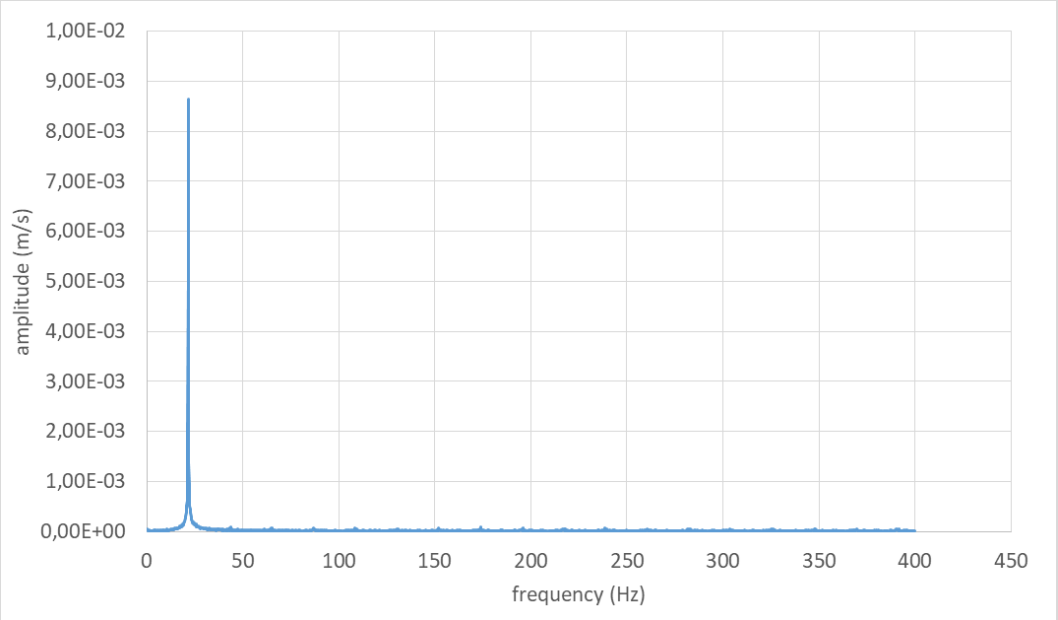

Figure 5.23. Impact test FFT result of lower CMG with electromagnets (21.75 Hz first fundamental frequency)

After mounting the electromagnets, it has been seen that there is no change in the fundamental frequencies. However, multiples of the fundamental frequencies almost vanished. The possible reason behind this may be Eddy currents developed inside the rotor and the electromagnets, and due to the movement of the ferromagnetic rotor body. These developed currents create a damping effect on the rotor and clear higher harmonics on the motion of the rotor. As a result, only the first fundamental frequencies remained.

Polar moment of inertia of the rotors becomes as follows after modification.

$$I_{rotor} = \begin{bmatrix} 951377.23e-9 & 0 & 0 \\ 0 & 951377.23e-9 & 0 \\ 0 & 0 & 20940.58e-9 \end{bmatrix} kg.m^2$$

Inertia value at the Z axis (spacecraft) is about 45 times smaller than the X and Y axes inertia values and manufactured rotor geometry closely satisfies optimum inertia distribution relation in Eq. (63).

The air bearing in the previous experiment failed due to rust and, a new air bearing was ordered to continue experimentation. The new air bearing is PI Glide A-632.050H model which includes a high-resolution encoder. It can carry 536 N axially and 229 N radially and operates with 75-80 Psi pressurized air. The encoder has 15,744 lines/rev on the scale, and the electronics provide 4x interpolation. In total, there are 62,976 encoder counts/revolution of the stage. Hence, the resolution of the encoder is 99.77 μrad.

A force transducer was also ordered to measure torque output of the actuator and it can also be assembled to balancing platform instead of the air bearing. The purchased force transducer is AMTI MC3A-250 multi-component force transducer and it can carry 556 N force on X and Y axes which correspond the gimbal and the rotor excitation axes of the actuator. 1112 N maximum load can be applied on the Z axis of the sensor. The gain and excitation voltages for 3 axis forces and moments can be adjusted by using AMTI Netforce software. Hence, force and torque resolution of the transducer can be adjusted for each axis. With maximum gain and excitation, resolution for measured torques drops down to 0.00014362 Nm/bit for the X and the Y axes and 0.00017952 Nm/bit for the Z axis. However, highest torques can be measured by the sensor drop to 1.18 Nm on the X and the Y, 1.47 Nm on the Z axes.

Firstly, experiments for torque characteristics were done by using the force transducer. Full view of experiment setup may be seen in Figure 5.24. There are eight electromagnets on the experiment prototype as mentioned before. Hence, eight driving signals must be generated. Because of manufacturing errors of mechanism and differences in generated signals due to varied properties of electrical circuits and electromagnets, the amplitude and phase difference of eight signals must be tuned precisely to generate desired motion of the rotors. The signals are generated via Raspberry Pi 3 B+ model small computer which runs with a Linux operating system. The wireless connection between Raspberry Pi and another computer established via remote control software. Signal generation code is written in the Python language. The generated signals are transferred PCF8591 YL-40 digital to analog converted modules

which communicate through i2c port of the Raspberry Pi with 400 kHz speed. Coming digital signal data from Raspberry were converted to analog signals by using these modules and analog signals were amplified with inverting amplifier circuits with On Semiconductor LA6500 power operational amplifiers.

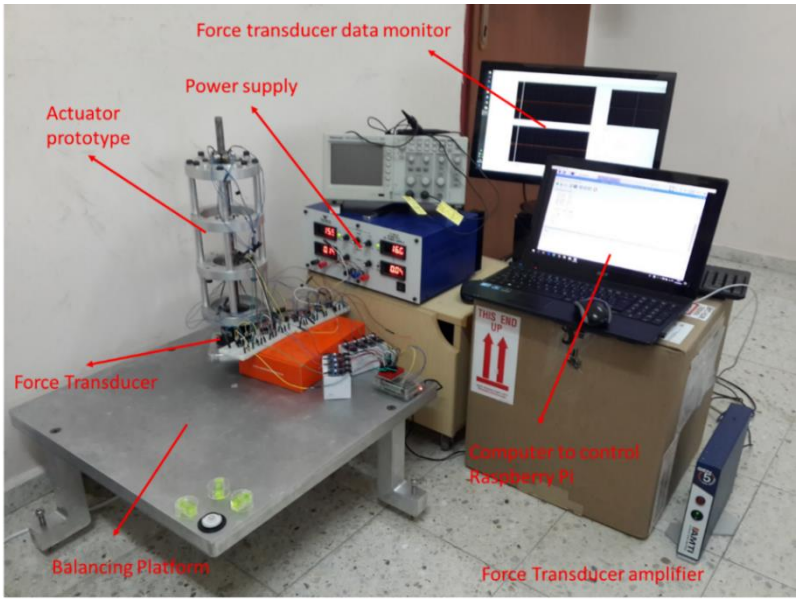

Figure 5.24. The general picture of the experiment setup with the force transducer

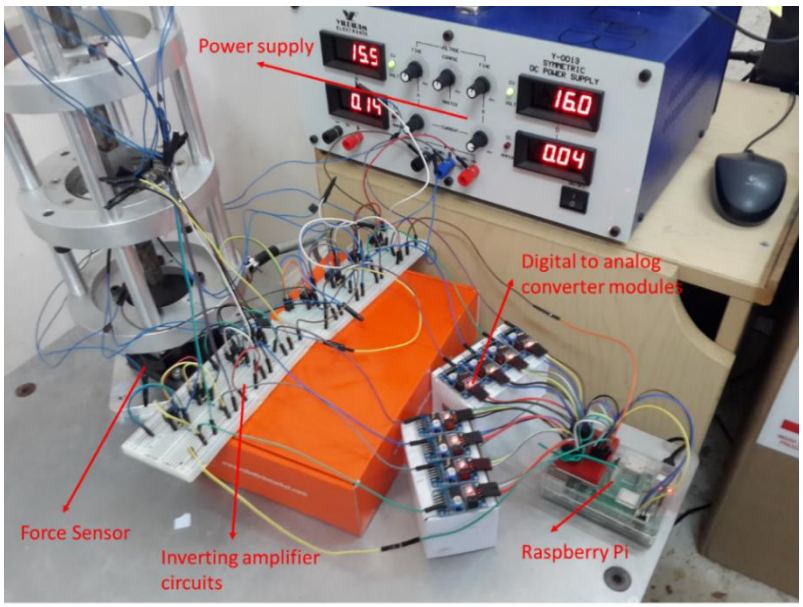

Figure 5.25. Electrical circuit layout

The electromagnets were driven with sine waves squeezed between zero voltages and desired maximum voltage. To have rotary motion mentioned on the rotors, the electromagnets were excited with 0°, 90°, 180°, and 270° phases. Therefore, signals go to their peak voltages sequentially. Hence, the electromagnets run sequentially as a rotary configuration. As a result, the rotor body does precession motion. The whole system was operated with open loop control.

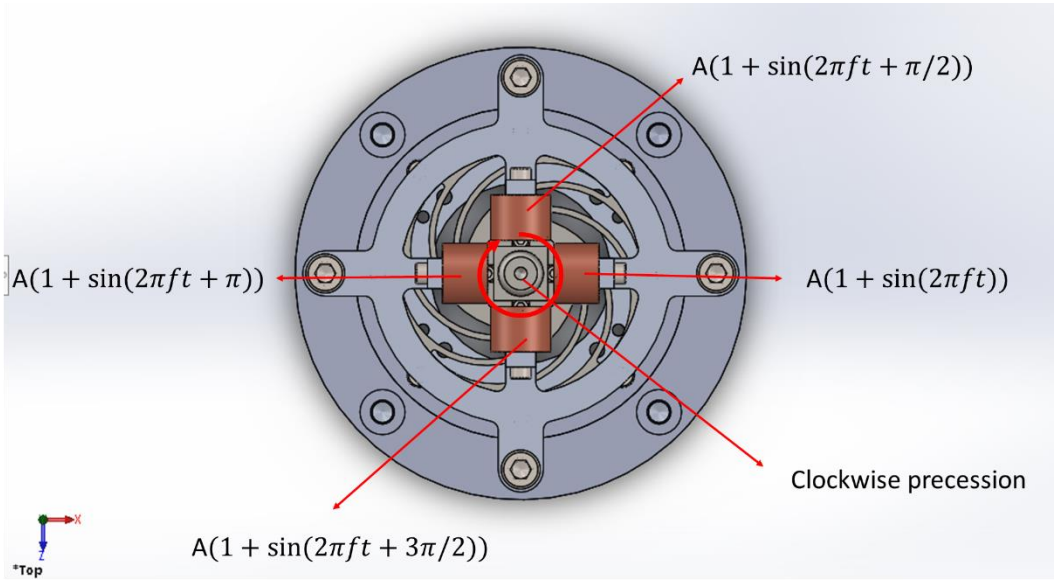

Figure 5.26. Driving signals for electromagnets and direction of precession for the ideal case

Firstly, the upper stage of the actuator was disassembled and only the output of the lower actuator was taken. Amplitude and phases of generated signals were slightly adjusted to have desired motion of rotor body. The amplitude of vibrations is 2.34°. The CMG was excited with 21.5 Hz frequency which is very close to the resonance frequency of flexure geometry. The steady-state torque output of a single actuator is represented in Figure 5.27. Data length is 0.2 seconds. There is 90° phase difference between X-axis and Y-axis response torques as expected.

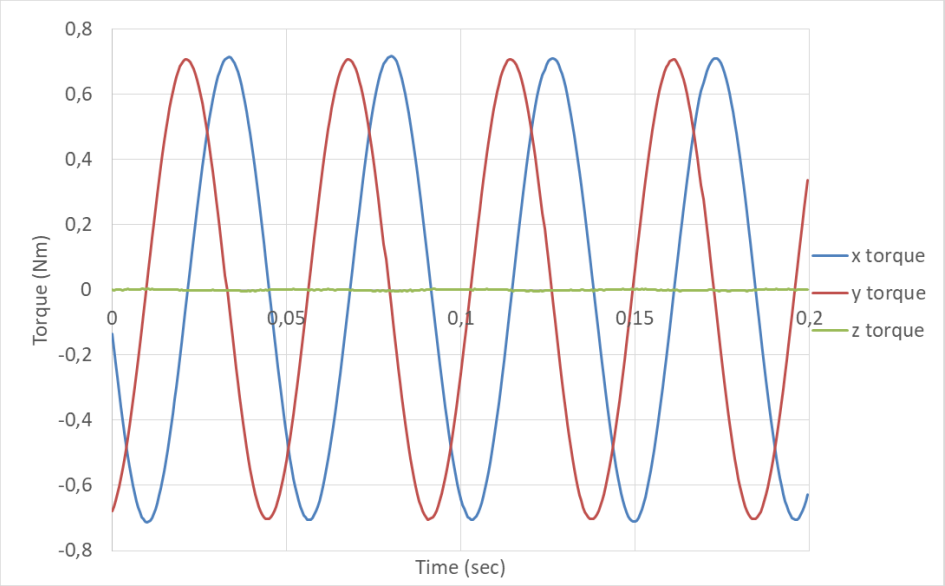

Figure 5.27. The steady-state torque output of the lower CMG

In more detail, only Z-axis torque output may be seen in Figure 5.28. The net torque on the spacecraft body is zero but a very slight oscillation has been observed with some amount of noise. When the smooth velocity output of the slender rotor considered in the simulation results, this result is also expected.

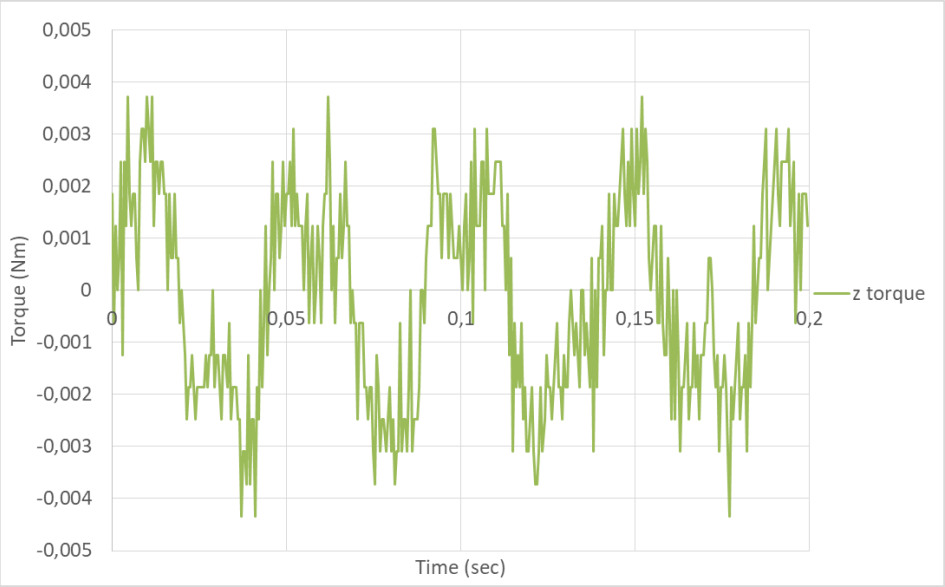

Figure 5.28. The steady-state torque output of the lower CMG on Z-axis

After adjustment of the excitation voltages and phases by using the force transducer, the whole system mounted on the air bearing to see angular velocity output of the actuator. The circuit components placed on the avionics plate and before mounting to the air bearing. The positions of the components were defined to balance weight distribution on the plate using the force transducer. Hence, the effect of gravity due to unbalance and tilt of the balancing platform may be reduced as low as possible.

Four Li-Po batteries were used as power supply for the amplifier circuits. These batteries have a capacity of 2200 mA.h and 7.4 volts with 2S configuration. Four of them were serially connected and from the middle of the serial connection, the circuit was grounded. When the batteries are fully charged, ±16.8 volts supplied from the battery set. Raspberry Pi was also powered with another battery with 5 volts 2.1 A output. Hence, the whole system becomes wireless for testing.

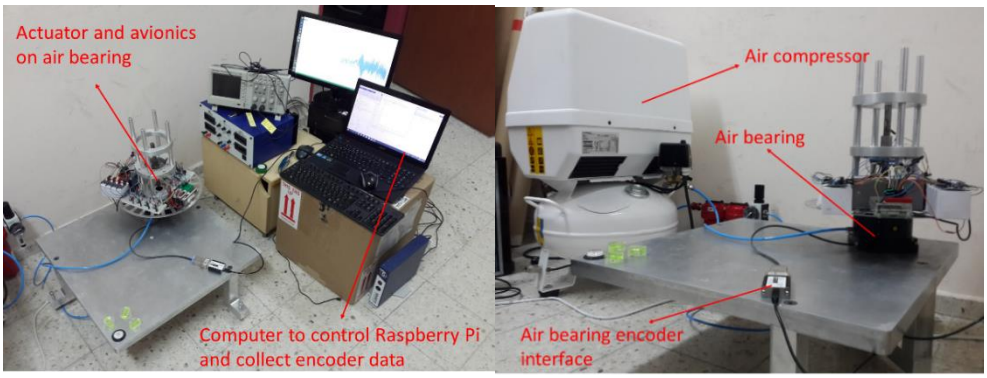

Figure 5.29. The general picture of the experiment setup for lower CMG mounted on the air bearing

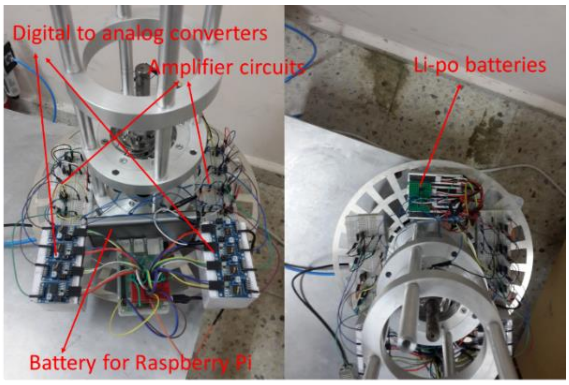

Figure 5.30. The positioning of electrical circuit components for a balanced distribution of mass

When the air bearing was pressurized, it has been seen that there occurs a turbine torque inside the air bearing and it starts rotating itself. Angular position data collected by the encoder for 40 psi pressure may be seen in Figure 5.31.

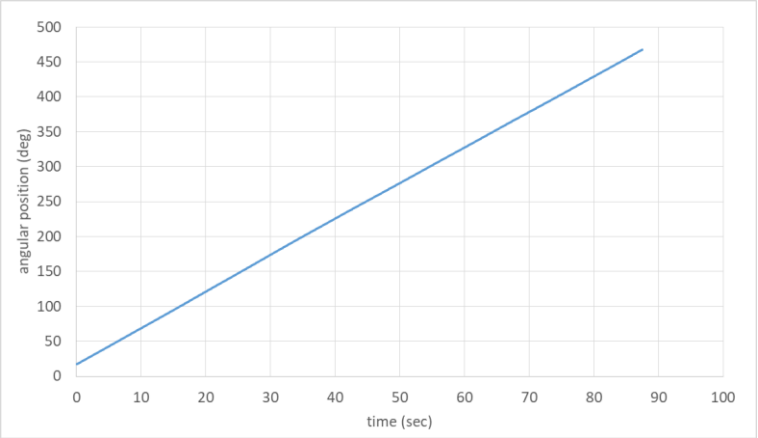

Figure 5.31. Change in angular position due to turbine torque inside air bearing

It may also possible to extract angular velocity gain from the bias caused by turbine torque. In order to do that, firstly detailed angular velocity profile of the air bearing investigated. It is concluded that, due to inner dynamics of bearing, there are unpredictable and unexpected velocity fluctuations during rotation caused by turbine torque and amplitude of oscillations are comparable to actuator output angular velocity amplitude (Figure 5.32). Hence, it is hard to extract angular velocity gain from this noisy bias.

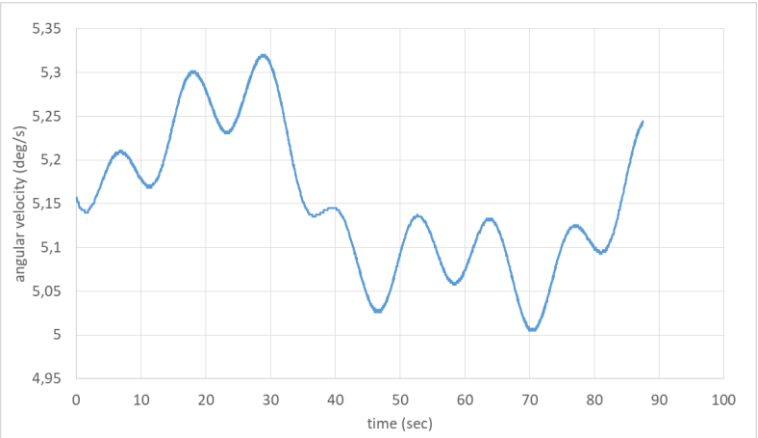

Figure 5.32. Turbine torque angular velocity of the air bearing under 40 psi supply pressure

In order to eliminate the turbine torque better, an experimental procedure was developed. Firstly, the air supply is completely closed and the air bearing becomes stationary. Then, it is opened small enough (around 10 psi) to just carry weight on the air bearing and the actuator is excited immediately after the air supply is opened. Hence, there was not enough time to gain velocity for the air bearing due to turbine torque. Thanks to this procedure, better experimental results were obtained.

The actuator was excited 21.5 Hz and amplitude of the vibrations are 2.34° for the rotor body. Total excitation time was 45 seconds and amplitudes of input voltages increased in 15 seconds in order to eliminate initial condition effects on the output angular velocity. The excitation signals were cut at 45th second after the start and the rotor body slows down under hysteresis damping forces inside the flexure geometry.

The air bearing was rotated about 8 degrees in 45 seconds and the angular position data collected by the encoder may be seen in Figure 5.33.

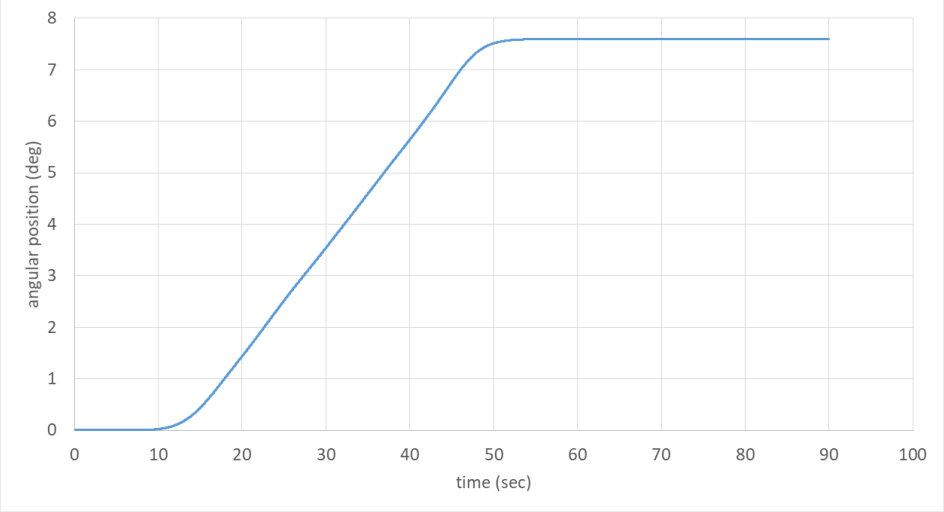

Figure 5.33. Angular position gain on air bearing axis with balanced masses and lowest possible turbine torque effect

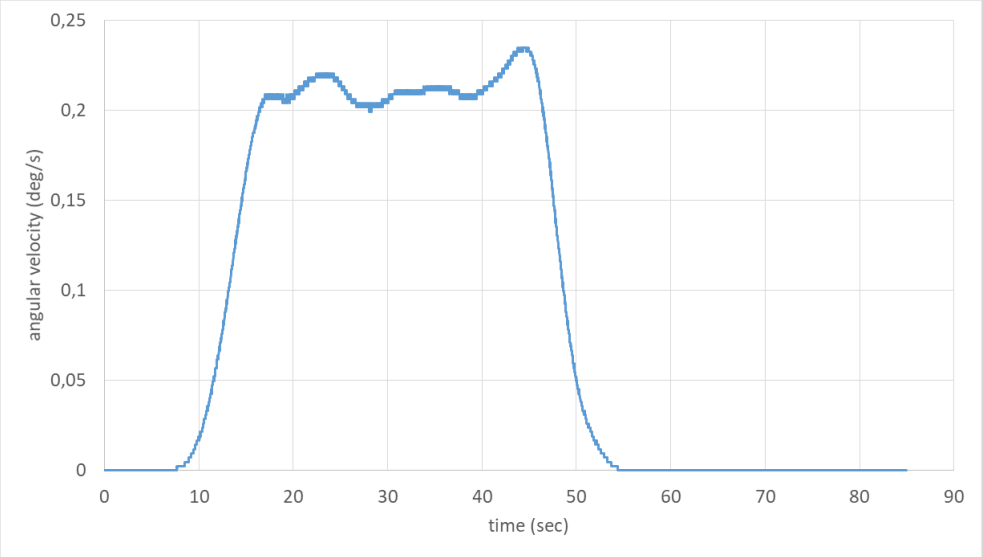

Figure 5.34. Angular velocity gain on air bearing axis with balanced masses and lowest possible turbine torque effect

The angular velocity gain slightly deviates in Figure 5.34. One of the reasons behind this may be the open loop control applied to rotors. The amplitudes of the rotor vibrations cannot be stable perfectly to have constant angular velocity gain. Secondly, the air bearing also has some dynamics inside due to air flow and the roughness of its surfaces. This may also affect the angular velocity output.

The most important observation of this part of the experiment is that the oscillations on the angular velocity are very small compared to the oscillations of the angular velocity in the previous experiment prototype with arbitrary rotor inertia values. The amplitude of oscillations is about 0.002°/s which is around 1% of the angular velocity gain. Actually, the resolution of encoder was not enough to detect these remaining small oscillations on velocity output. As a result, it may be concluded that the velocity oscillations were less than 0.002°/s and Figure 5.35 shows measurement noise. This result is expected when the output torque result of the Z-axis of the force transducer in Figure 5.28.

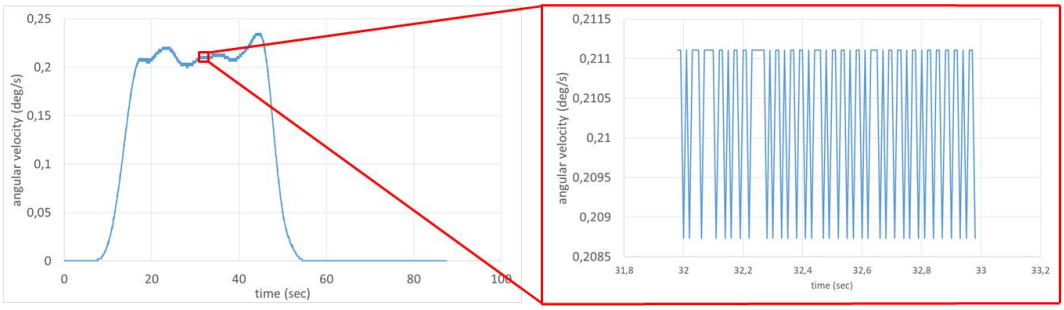

Figure 5.35. Oscillations on angular velocity gain between 32nd and 33rd seconds of the result in the previous figure

When the phase differences given to electromagnets were reversed, the direction of motion changed as expected. As a result, a similar angular velocity gain trend was obtained with reversed direction of motion.

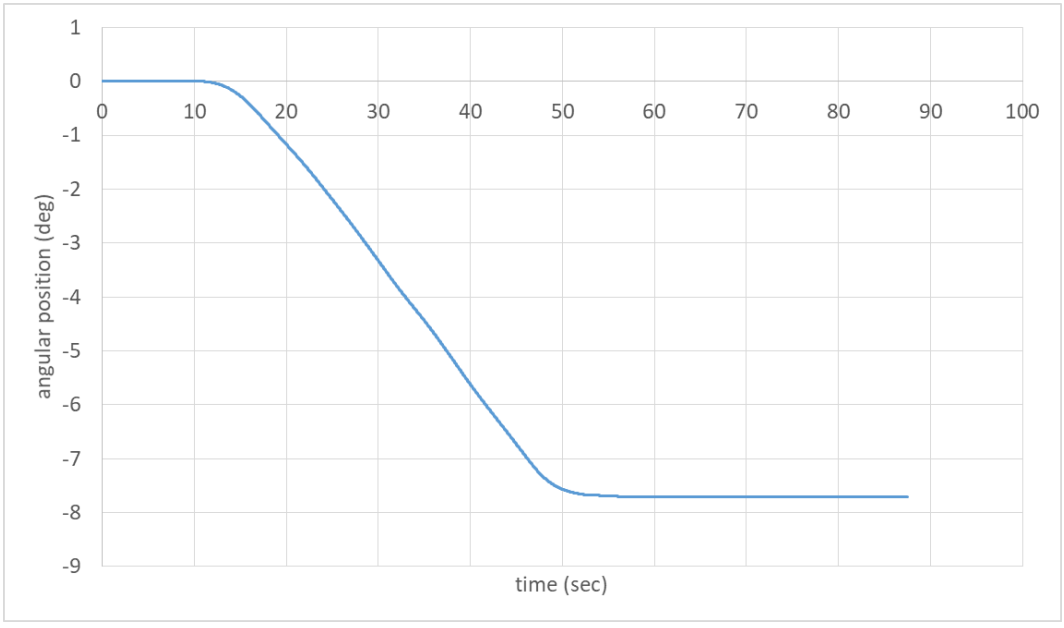

Figure 5.36. Angular position gain on air bearing axis with balanced masses and lowest possible turbine torque effect (reversed direction)

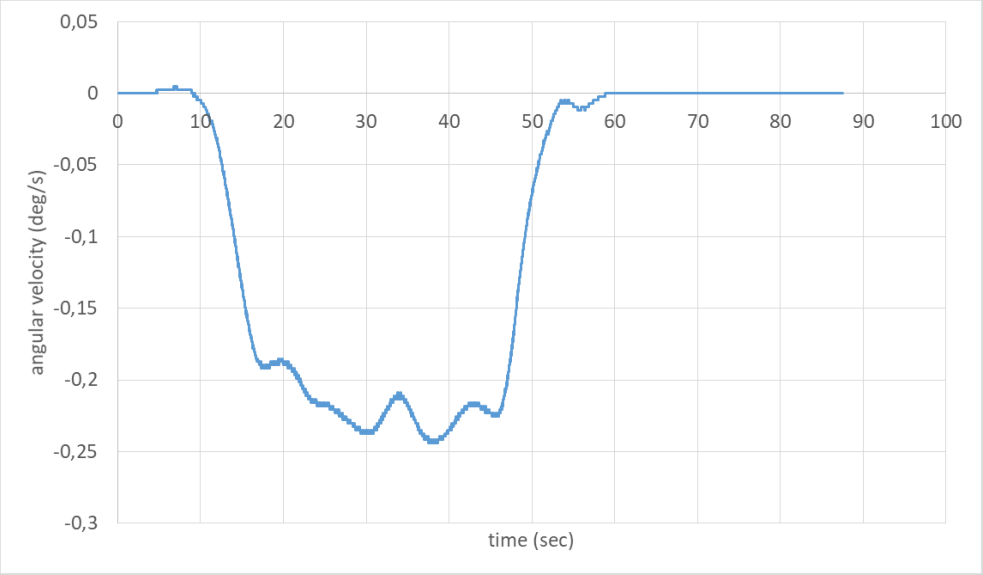

Figure 5.37. Angular velocity gain on air bearing axis with balanced masses and lowest possible turbine torque effect (reversed direction)

Both positive and negative directions resulted in almost the same position gain around 8 degrees of rotation in 45 seconds.

A pair of CMG configuration was also tested on the force transducer for the output torques. Previously, it was proposed that a pair of CMGs may cancel out excitation vibrations on X and Y axis. Two rods were driven synchronously to demonstrate this effect.

Upper and lower CMGs were excited separately at the beginning of the tests. However, it was hard to synchronize two rods with out of phase manner by using open loop control. Hence, a flexible coupling was mounted to ends of the rods for out of phase motion. Thanks to this coupling, tips of the rods were connected and they started moving together. The mounted coupling can easily be bent on X-axis and Y-axis and it can easily be deflected on Z-axis. However, it restricts the translational motion of the rods with respect to each other on X and Y axes. Due to mounted coupling, there occurred an unbalance on the rotor bodies. These unbalance also caused vibrations on X and Y axis. As a result, balancing masses added to other two ends of the rods and their amounts were tuned to decrease excitation response torques as low as possible.

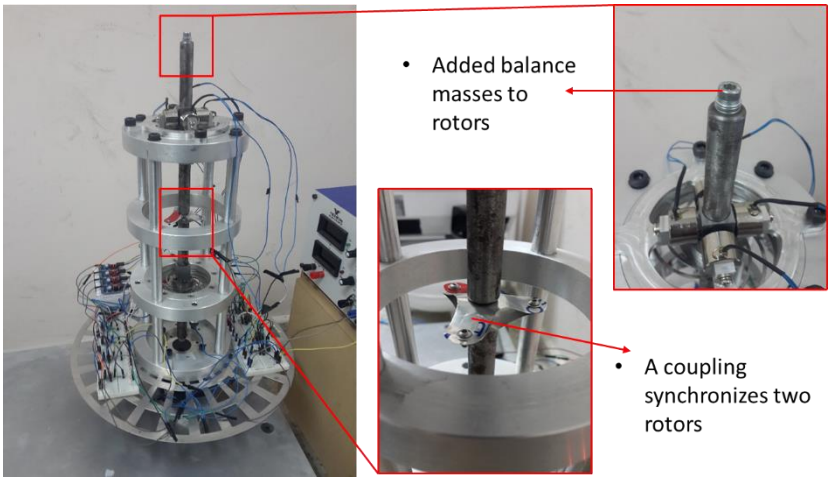

Figure 5.38. Flexible coupling mounted between two rods and mounted balance masses added to the other tips of the rods

The torque output results of this configuration may be seen in Figure 5.39. The amplitude of vibration of two rods measured as 1.34° and corresponding torque generated by single CMG calculated as 0.39 N.m. Hence, generated excitation torques by individual CMGs on X and Y axis was dropped from 0.39 Nm to 0.06 Nm and 0.035 Nm, respectively. This result shows that the proposed CMG configuration is successful to reduce excitation vibrations. It is possible to reduce this remaining vibration even more with high precision manufacturing and closed-loop control algorithm.

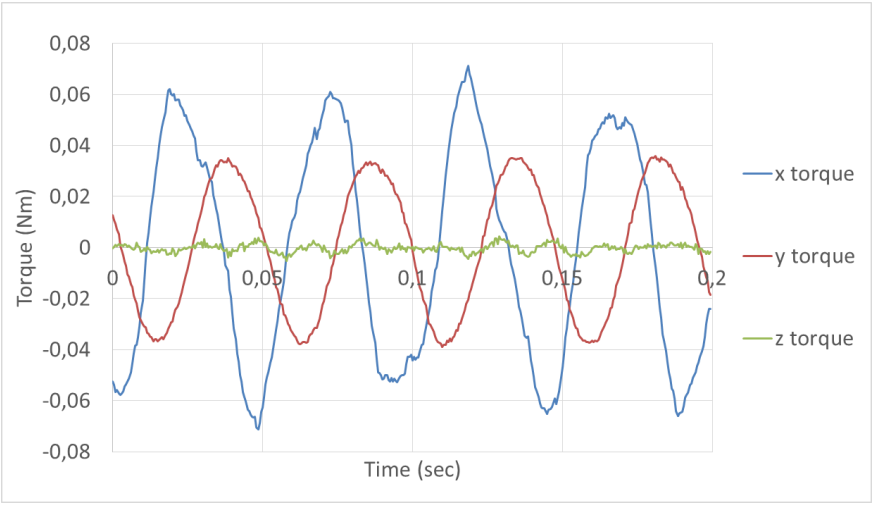

Figure 5.39. The torque output of a pair of CMG configuration

CHAPTER 6

CONCLUSION AND FUTURE WORK

In this thesis, the concept of a novel satellite attitude control actuator based on rotational vibrations is presented.

Developing a detailed mathematical model and simulating it, it has been proved that vibratory CMG concept gives useful rotational motion to spacecraft on desired rotation axis. The single gimbal CMG model was used for the mathematical model of the concept and then output angular velocity equations are obtained using conservation of the angular momentum principle.

Effects of excitation parameters such as excitation frequency, excitation amplitudes and the phase difference between rotor and gimbal excitation axes were investigated and the following results are obtained.

- The angular velocity output increases proportional to the excitation frequency.
- The angular velocity of the spacecraft increases in a quadratic manner with increasing excitation amplitudes of rotor and gimbal bodies.
- The angular velocity output is directly proportional to sine of phase difference between the rotor and the gimbal excitations.

For 0º, 180º and 360º phase differences between rotor and gimbal axes, the spacecraft only vibrates around its original orientation and there is no net angular displacement on the desired rotation axis. The maximum angular velocities are obtained at 90º and 270º phase differences. Both the magnitude and direction of the angular velocity may be controlled by changing the phase difference between [-90º, 90º].

There are also vibrations on the other two axes of the spacecraft reference frame due to the reaction forces and moments of the rotor and the gimbal bodies. When the amplitudes of reaction angular velocities on X and Y-axes were compared with the

angular velocity output magnitudes, it has been observed that these reaction angular velocity amplitudes are very high and they must be canceled. Hence, a double CMG configuration was proposed to cancel out these oscillatory motions on the other two axes of the spacecraft. Two CMGs were driven out of phase manner and they cancel out excitation vibrations of each other, leaving only the desired rotation at the output axis.

The angular velocity output on the desired rotation axis also has oscillations and it is observed that the reason of these oscillations is axisymmetric rotor geometry such as a cylinder, cube or sphere. Mathematically, optimum rotor inertia distribution relation was also investigated to reduce these velocity oscillations to a minimum. This result of this study is one of the most important and novel contribution of this thesis. Detailed analysis of rotor inertia distribution was tabulated. It is shown that when the rotor body evolves to a slender rod geometry,

- The angular velocity increases for the same rotor mass
- The velocity fluctuations decrease. Therefore, the velocity profile becomes smoother. Smooth operation of the actuator is important for some operational purposes such as image capturing by Earth observation satellites.
- These results also mean that it is possible to achieve the same angular velocity with less rotor mass. Hence, it is beneficial for reducing the total mass of the actuator and the spacecraft.

Kinematic analysis of the motion of the slender rotor body was also performed to understand motion under different phase shifts between the rotor and gimbal excitation. The tip point of the rod geometry draws a circular path for 90º phase difference. This path slightly deviates from an exact circle as the excitation amplitudes increase. Hence, it was concluded that the rotor geometry actually does precession motion when 90º phase difference applied between the rotor and gimbal excitation.

Before the optimum inertia distribution for rotor body was discovered, a preliminary mechanical design with arbitrary rotor inertia values had been performed and tested. Effect of phase difference was proved with experimental results which show the same trend and behavior with the results of the mathematical model.

At the final stage, a new mechanical design with slender rod rotor geometry was studied. A balance platform to reduce gravitational effects was also designed and manufactured. This new mechanical design consists of two actuators, without the gimbal body because it has been shown that the gimbal body does not contribute the angular velocity output on the desired rotation axis. Instead of the mechanical gimbal, a flexure geometry was designed. Hence, the rotor body has two rotational degrees of freedom. Rotor bodies were excited by electromagnets. Hence, this mechanical design does not have any joints and there is no contact to drive rotor bodies.

Several experiments were done on both force transducer and the air bearing to observe system dynamics. Firstly, upper CMG is removed from the design and only single CMG outputs were obtained. Experiment results showed that angular velocity direction changes when phase differences are inverted (Figure 6.1). Moreover, angular velocity fluctuation drastically reduced and air bearing rotated more smoothly. This result shows that the slender rod geometry mitigates angular velocity oscillations on the desired rotation axis. Secondly, two slender rods were excited together on the force transducer to observe output torques of the actuator. The excitation torques on X and Y axes reduced considerable amount compared with excitation response torques of single CMG. Clearly, a pair of CMG configuration successfully reduces excitation response torques on the spacecraft body.

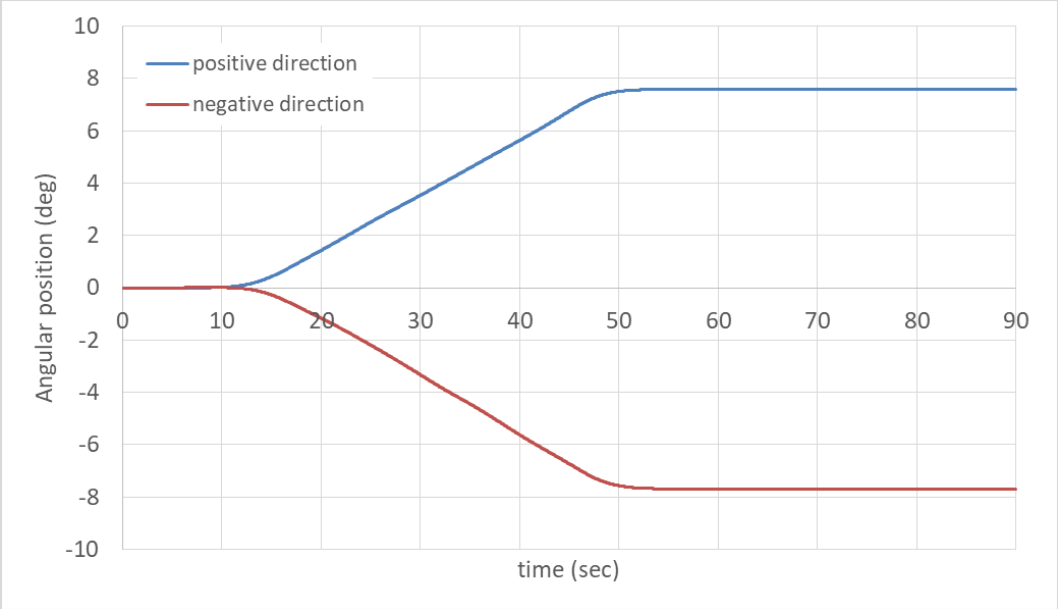

Figure 6.1. The positive and negative direction of rotations for a single CMG

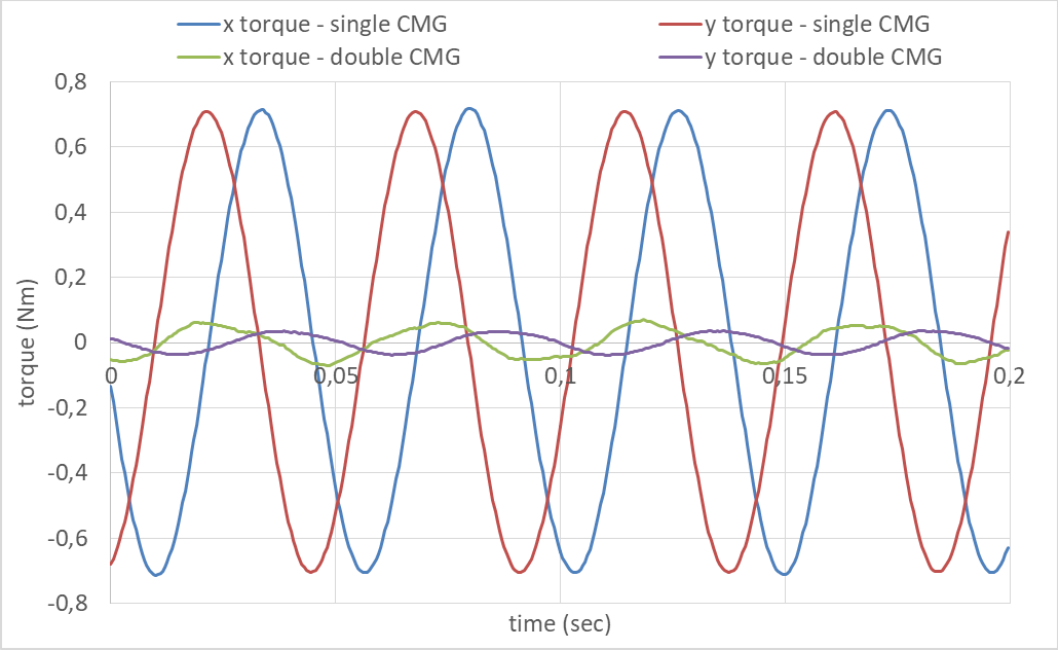

Figure 6.2. Comparison of the excitation response torques of a single CMG and a pair of CMGs

As a future study, the closed-loop control algorithm can be applied to this mechanical design to achieve maximum output velocity and minimum parasitic vibrations. The motion of the rotors may be detected by MEMS gyros or the Hall Effect sensors and a feedback control algorithm can drive the electromagnets accordingly.

In addition, MEMS version of this concept can be performed. Angular momentum storage capacity of a single rod for macro scale actuator is relatively small. As a result, the performance of the single actuator at macro scale is not comparable with the performance of reaction wheels and conventional CMGs. However, an array of microscale design which consists of a large number of actuators may have comparable performance. Detailed performance analysis of MEMS arrays of this concept can be performed for future study.

REFERENCES

[1] ESA, "ECSS E-HB-60A Control Engineering Handbook," European Cooperation on Space Standardization, 2010.

[2] J. J. Lissauer and I. d. Pater, Fundamental Planetary Science: Physics, Chemistry, and Habitability, Cambridge University Press, 2013.

[3] J. Lang, "Gyroscopic control". US Patent 1,096,253, 1914.

[4] E. A. Sperry, "Ship stabilizing and rolling apparatus". US Patent 1,232,619, 1917.

[5] R. Goddard, "Gyroscopic steering apparatus". US Patent 2,158,180, 1936.

[6] R. Votel and D. Sinclair, "A comparison of CMGs and reaction wheels for small earth observing satellites," in *26th Annual AIAA/USU Conference on Small Satellites*, 2012.

[7] T. Coon and J. Irby, "Skylab attitude control system," *IBM Journal of Research and Development,* pp. 58-66, 1976.

[8] E. H. Fikes, "Control moment gyro for skylab," NASA Technical Memorandum, 1971.

[9] B. Corporation, "Atm CMG bearing failure analysis final report," NASA Technical Memorandum, 1975.

[10] D. S. F. Portree, "Mir hardware heritage," NASA Technical Report, 1995.

[11] L. K. Erickson, Space Flight: History, Technology, and Operations, Lanham, Maryland, USA: The Scarecrow Press Inc., 2010.

[12] V. P. Legostaev, "Russian space programs: Achievements and prospects of automatic control applications," *Annual Reviews in Control,* pp. 1-11, 2005.

[13] D. S. Airbus, "Cmg 15-45s. datasheet," 2018.

[14] M. A. Gleyzes, L. Perret and P. Kubik, "Pleiades system architecture and main performances," in *XXII ISPRS Congress*, Melbourne, Australia, 2012.

[15] J. Reiter, K. Bohringer and M. Campbell, "Mems control moment gyroscope design and wafer-based spacecraft chassis study," in *Proceedings of SPIE*, 1999.

[16] H. Chang, W. Jiao, Q. Fu, J. Xie and W. Yuan, "Design and simulation of a mems control moment gyroscope for the sub-kilogram spacecraft," *Sensors,* pp. 4130-4144, 2010.

[17] E. R. B. Stoneking, "Satellite GN&C Anomaly Trends," in *26th Annual AAS Guidance and Control Conference*, Breckenridge, CO, USA, 2003.

[18] J. K. Wayer, J.-F. Castet and J. H. Saleh, "Spacecraft attitude control subsystem: Reliability, multi-state analyses, and comparative failure behavior in LEO and GEO," *Acta Astronautica,* pp. 83-92, 2013.

[19] N. S. Tyrell and A. E. Hosoi, "Attitude Control via Structural Vibration," in *XXIV ICTAM*, Montreal, Canada, 2016.